Science
AAAS

Supplementary Materials for

Dual-polarity voltage imaging of the concurrent dynamics of multiple neuron types

Madhuvanthi Kannan *et al*.

Corresponding authors: Madhuvanthi Kannan, mkannan@umn.edu; Ganesh Vasan, gvasan@umn.edu; Mark J. Schnitzer, mschnitz@stanford.edu; Vincent A. Pieribone, vincent.pieribone@yale.edu

Science **378**, eabm8797 (2022)
DOI: 10.1126/science.abm8797

The PDF file includes:

Other Supplementary Material for this manuscript includes the following:

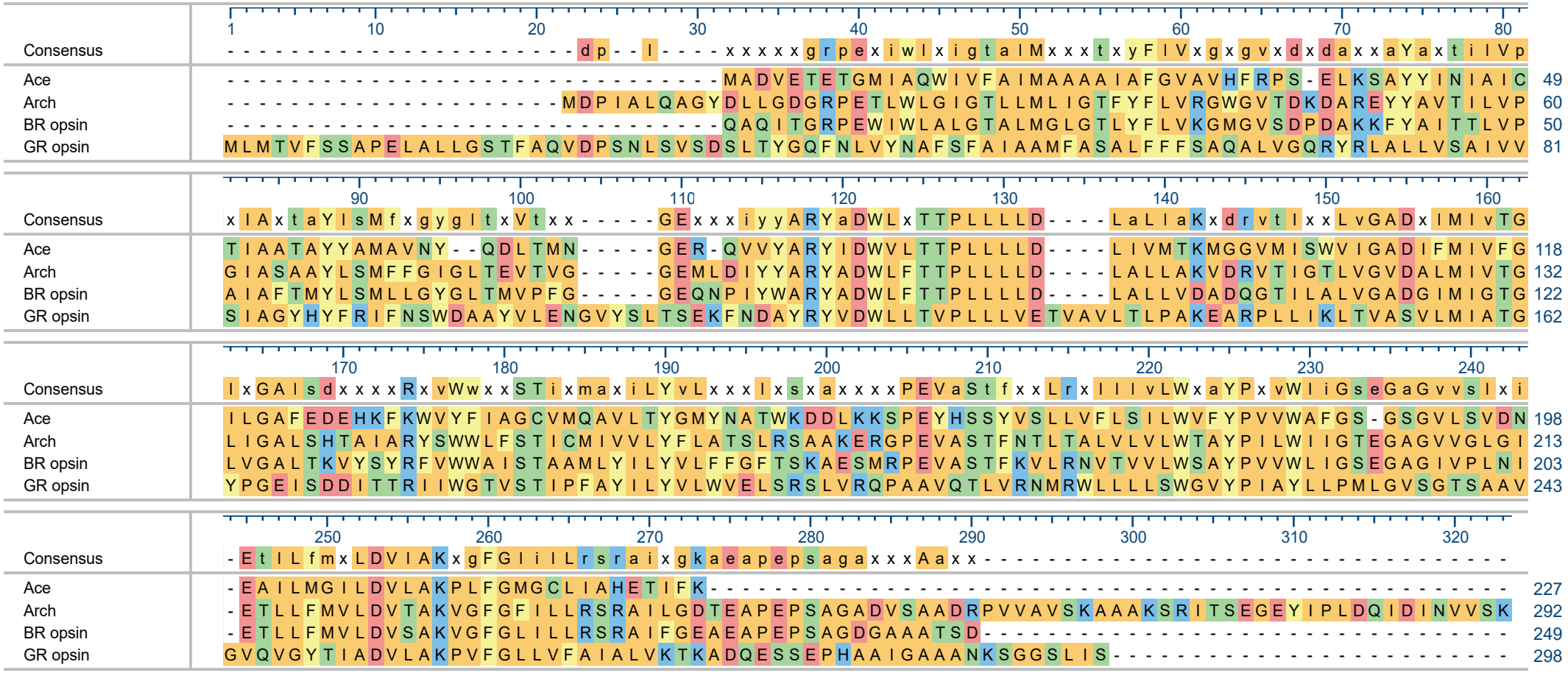

Figure S1 | Alignment of amino acid sequences of *Acetabularia* rhodopsin II (Ace), Archaerhodopsin (Arch), bacteriorhodopsin (BR) and *Gloeobacter* rhodopsin (GR). Boxes indicate residues targeted for site-directed saturation mutagenesis. AAs are color-coded based on side-chain chemistry. Conserved residues are indicated in upper case.

A Ace N81X mutagenesis in Ace-SY-mNeon

	1	2	3	4	5	6	7	8	9	10	11	12
A	-10 N81H	-3 N81I	0 N81A	-4 N81L	-2 N81P	-4 N81P	-3 N81N	-4 N81P	0 N81I	-5 N81N	-6 N81R	-8 N81S
B	-3	-2	-3	-8	-2	-4	-8	-4	-2	-12 N81A	-10	-3
C	-7	0	-18 N81S	0	-11	-3	-10	-10	-9	-5	-14 N81S	0
D	-14 N81F	-2	-16 N81S	-8	-8	-7	-11	-3	-5	-11 N81S	-6	Control

B Ace-FP linker mutagenesis in Ace-mNeon 81S (well C3 from above) (G229X)

	1	2	3	4	5	6	7	8	9	10	11	12
A	-25 G229G	-16 G229P	-13 G229E	-14 G229P	-15	-18 G229E	-17 G229S	-18	-20 G229H	-25 G229K	-17	-16
B	-17	-15	-17	-18 G229T	-12	-15	-12	-10	-21 G229F	-12	-13	-18
C	-14	-13	-10	-24 G229F	-10	-15	-11	-5	-18 G229F	-14	-16	-8
D	-16	-17	-6	-12	-12	-8	-9	-9	-18 G229F	-34 G229Y	-5	-25 G229W

C Ace-FP linker mutagenesis in VARNAM Δ229 Δ230 (G231X)

	1	2	3	4	5	6	7	8	9	10	11	12
A	-17 G231S	-26 G231I	-14 G231D	-22 G231T	0 G231Q	-16 G231A	-10 G231E	-18 G231M	-8 G231P	-19 G231K	-16 G231A	-16 G231S
B	-20 G231L	-16 G231D	-18 G231M	-15 G231Q	-18 G231C	-15 G231T	-11 G231A	-18 G231F	-20 G231L	-17 G231R	-12 G231G	-23 G231T
C	-16 G231S	-21 G231K	-8 G231P	-12 G231D	-15 G231A	-17 G231C	-15 G231F	-20 G231K	-18 G231L	-15 G231E	-23 G231L	-18 G231N
D	-20 G231Q	-20 G231K	-17 G231M	-18 G231L	-17 G231S	-16 G231W	-17 G231F	-19 G231F	-18 G231M	-15 G231G	-16 G231E	Control

Figure S2 | High-throughput screening for voltage sensitivity of Ace-mNeon2 and VARNAM.
(A) 48 variants containing saturation mutations at Ace N81 on the backbone of Ace-mNeon were each transfected in electrically excitable HEK cells (*30,31*) and screened for voltage sensitivity on the high-throughput platform (*18*). The maximum %Δ*F/F* obtained for each variant across 4 independent rounds of screening are indicated in each well, together with the sequence information, where available. Color density corresponds to the size of the signal in the negative direction.
(B) Same as (A) for Ace-FP linker mutagenesis on Ace-mNeon 81S backbone.
(C) Same as (A) for Ace-FP linker mutagenesis on VARNAM backbone.

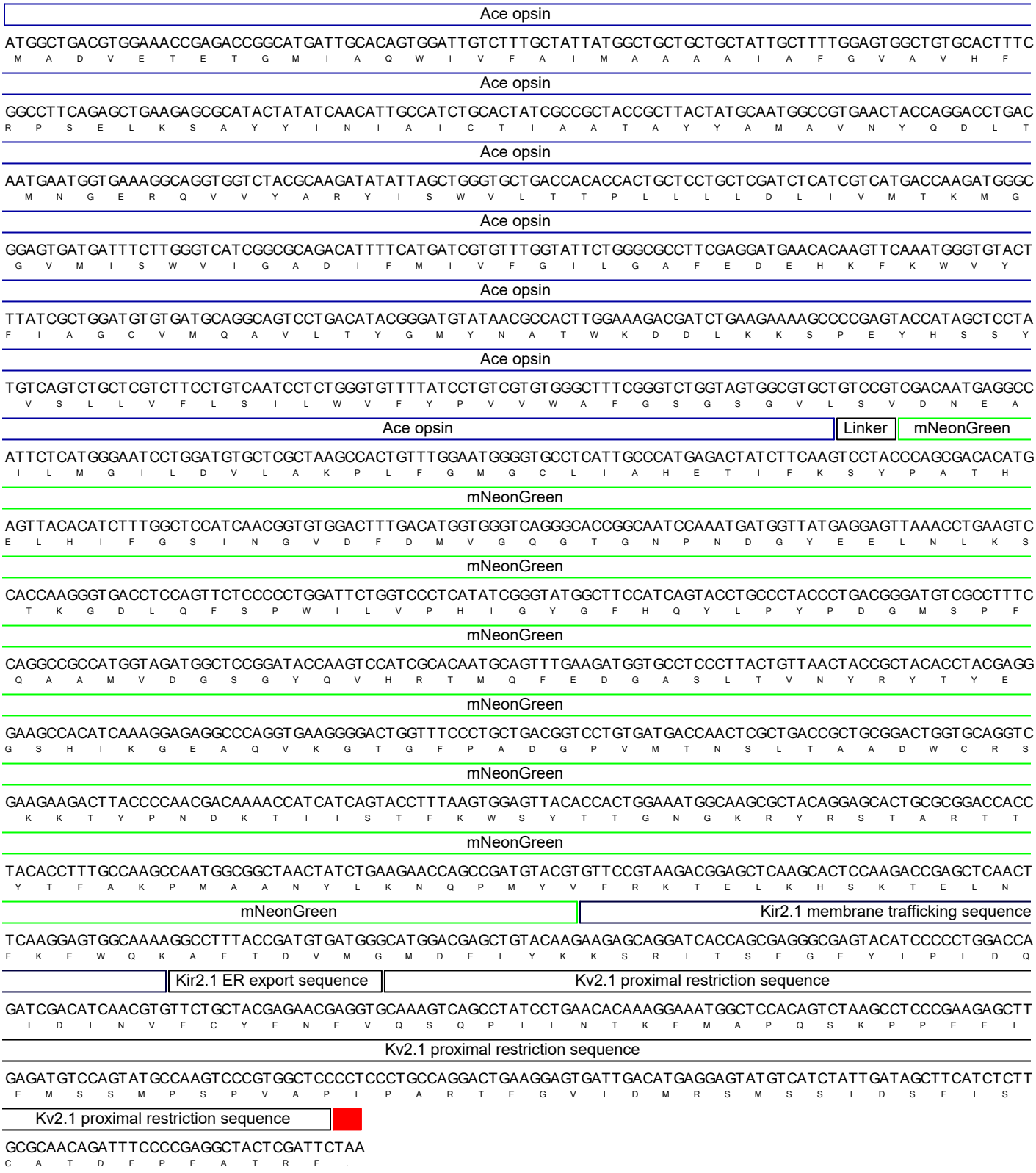

Figure S3 | DNA and amino acid sequences of Ace-mNeon2 fused to a somatic restriction sequence from Kv2.1.

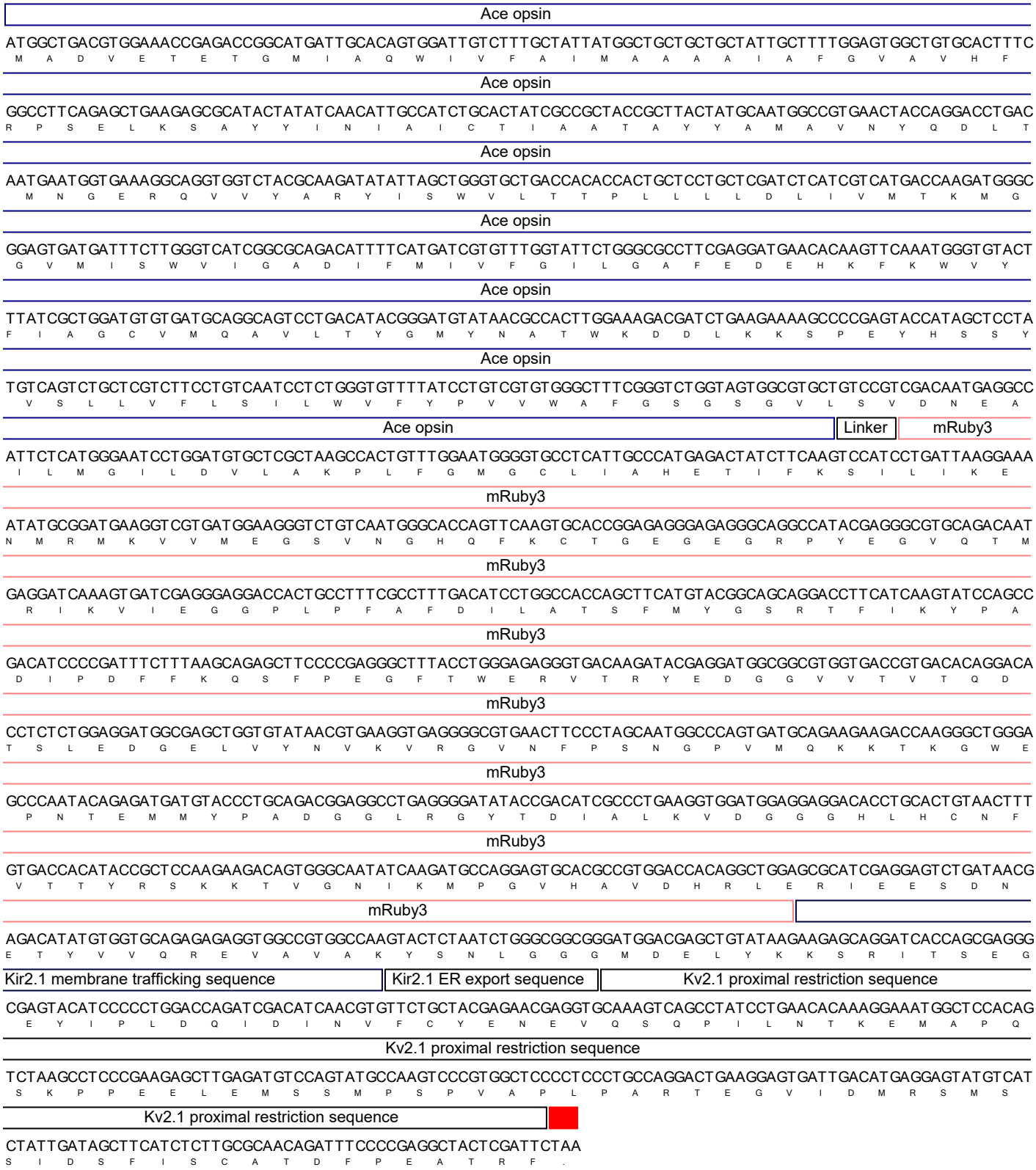

Figure S4 | DNA and amino acid sequences of VARNAM2 fused to a somatic restriction sequence from Kv2.1.

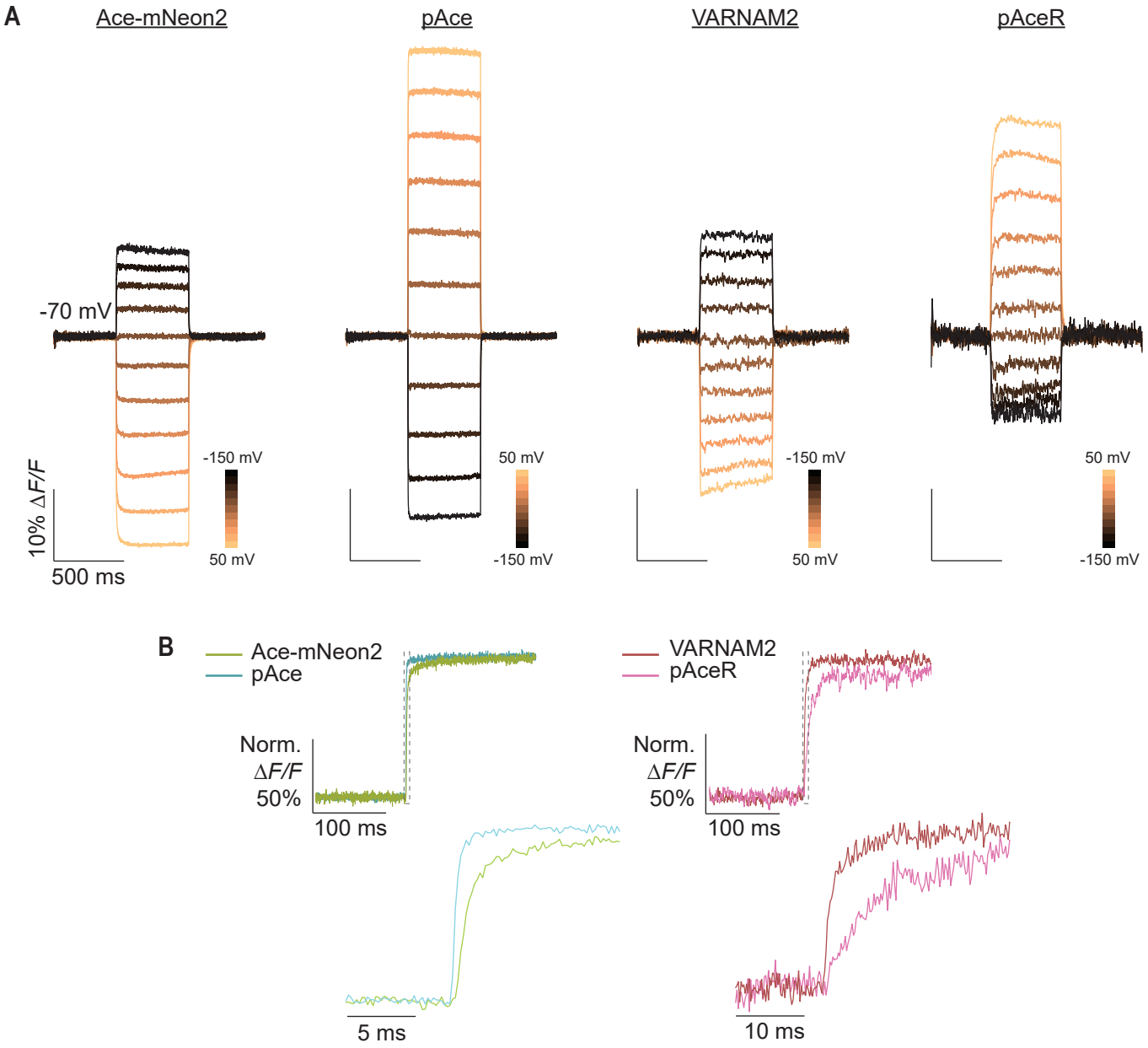

Figure S5 | Voltage sensitivity and kinetics of the four FRET-opsin indicators in HEK cells. (A) Example fluorescence responses from a HEK cell expressing Ace-mNeon2, pAce, VARNAM2 or pAceR during whole-cell voltage clamp recordings. HEK cells were held at -70 mV and responses were recorded to depolarizing and hyperpolarizing voltage steps at 20 mV increments. (B) Normalized fluorescence responses of HEK cells transfected with Ace-mNeon2 or pAce (*left*), and VARNAM2 or pAceR (*right*) during 120 mV depolarization. Dashed grey box represents interval shown below at an expanded time scale. Imaging conditions: 505 nm LED for Ace-mNeon2 and pAce and 565 nm LED for VARNAM2 and pAceR, 25 mW mm^{-2} at sample plane; image acquisition: 1 kHz.

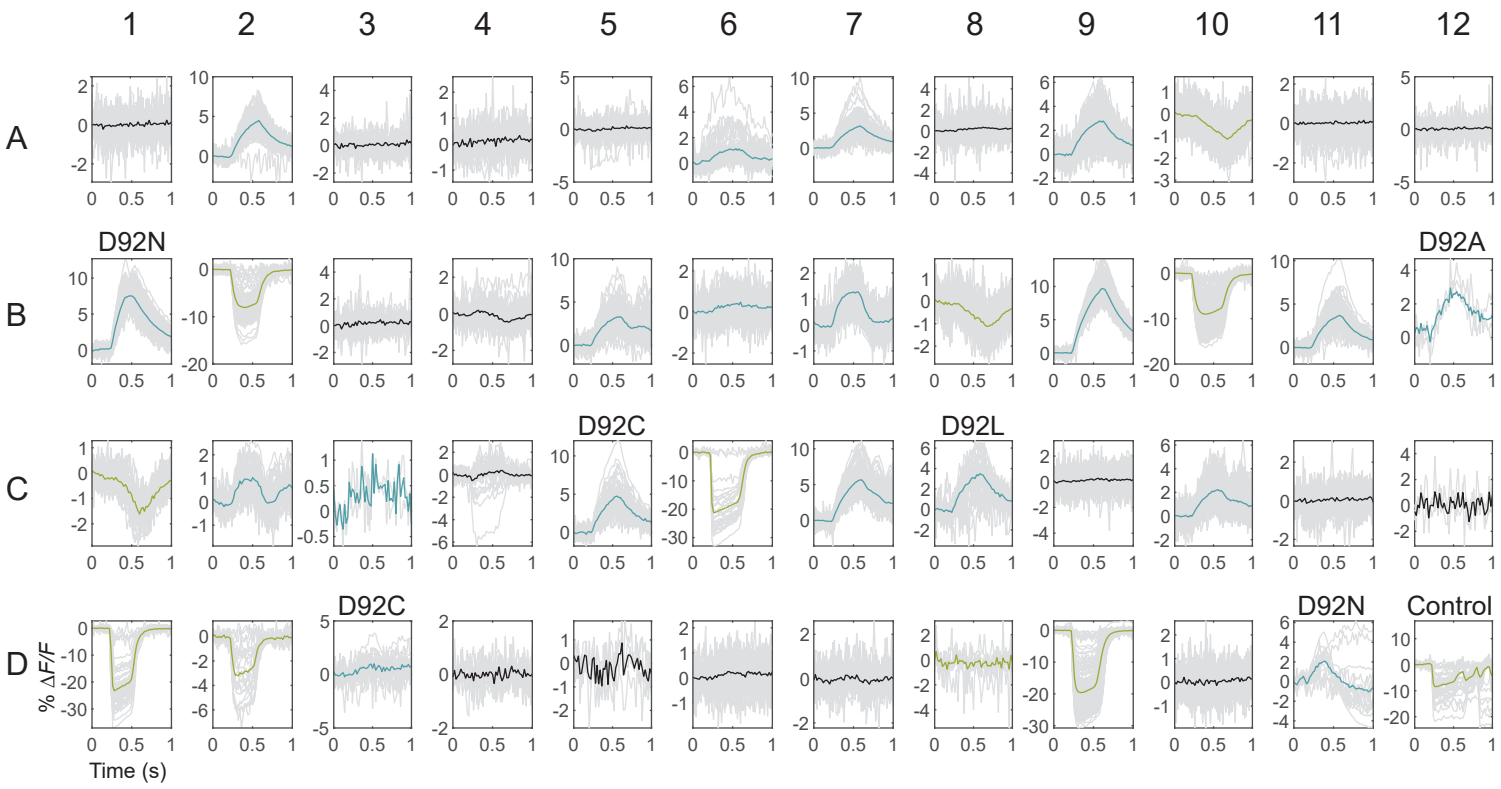

Figure S6 | High-throughput voltage screening of Ace-mNeon2 D92X mutants. 48 variants containing saturation mutations at Ace D92 were each transfected in electrically excitable HEK cells (*30,31*) and screened for voltage sensitivity on the high-throughput platform (*18*). Shown here are representative fluorescence responses of all cells (grey) from one field-of-view and one round of screening per variant. The average responses to depolarizing field potentials are indicated in blue for positive-polarity, green for negative-polarity and black for non-responding variants. Mutational information is indicated on top of each well for the positive-polarity variants, which were chosen for sequencing post-screening. (n>100 cells/variant).

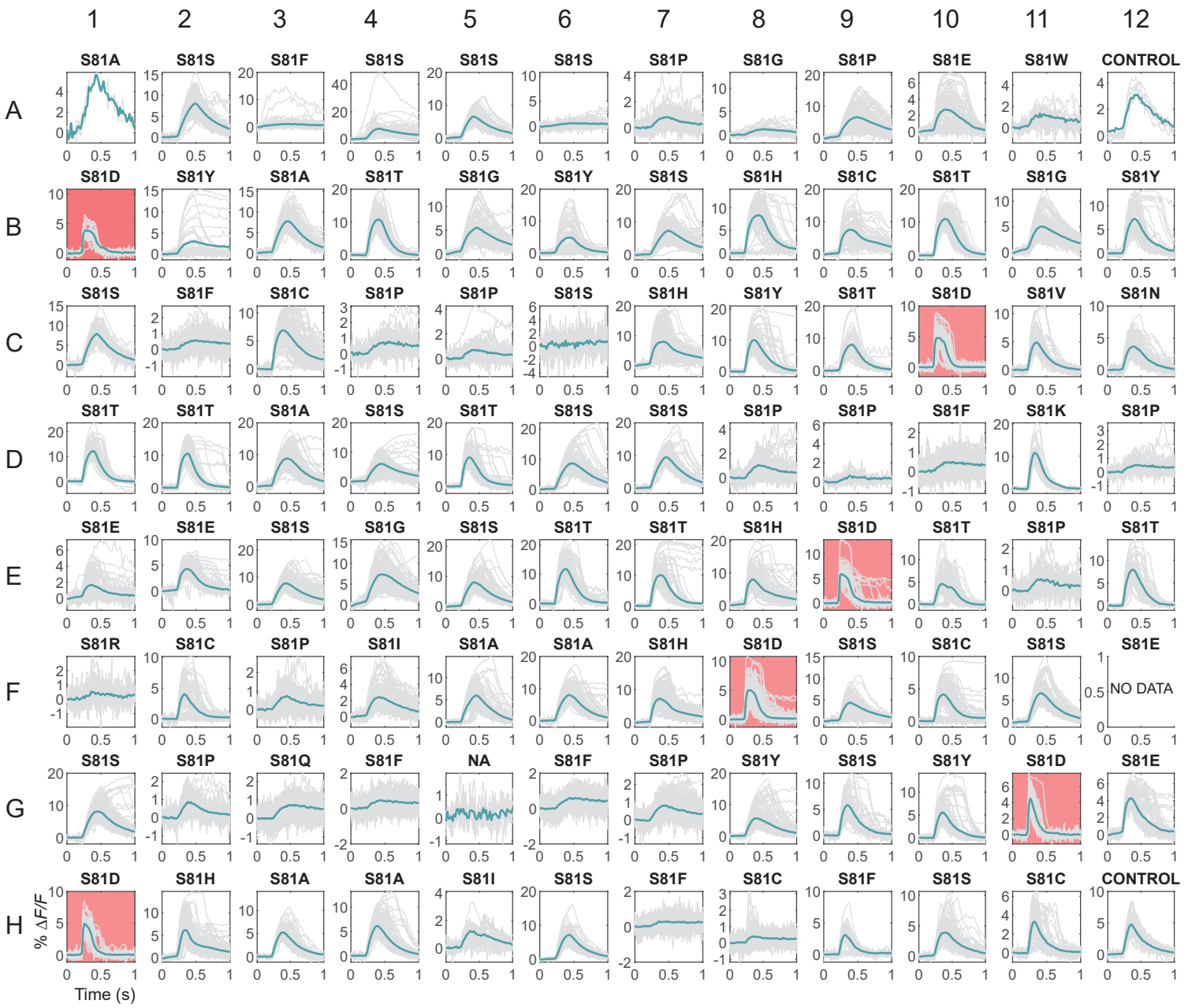

Figure S7 | High-throughput screening for kinetics rescue mutations in Ace-mNeon2 D92N. 96 variants containing saturation mutations at Ace S81 were each transfected in electrically excitable HEK cells (*30,31*) and screened for voltage sensitivity and response kinetics on the high-throughput platform (*18*). Shown here are representative fluorescence responses of all cells (grey) from one field-of-view and one round of screening per variant. The average responses to depolarizing field potentials are indicated in blue. Mutational information is indicated on top of each well (n>100 cells/variant except A1 and A12, where n<10 cells/well). Wells shaded in pink exhibited improvements in response kinetics, which is more conspicuous in the maximum response traces. Images were acquired at 200 Hz for this experiment (see Methods).

A Ace R78X and W178X on Ace-mNeon2 S81D D92N

	1	2	3	4	5	6	7	8	9	10	11	12
A	6 R78V	6 R78A	8 R78F	27 R78X	9 R78V	7 R78L	27 R78C	3 R78W	7 R78Q	6 R78S	1 R78F	Control
B	6 R78H	13 R78M	8 R78G	8 R78W	6 R78Y	2 R78Y	3 R78Y	10 R78M	37 R78K	43 R78K	6 R78V	7 R78L
C	8 R78R	8 R78W	8 R78S	10 R78R	0 R78W	35 R78K	2 R78W	3 R78A	3 R78C	2 R78Y	4 R78L	5 R78V
D	1 R78W	8 R78L	8 R78G	0 R78D	8 R78I	2 R78Y	2 R78W	7 R78R	2 R78C	4 R78Y	3 R78C	15 R78N
E	5 W178A	10 W178	8 W178W	5 W178A	4 W178K	2 No data	10 W178W	4 W178M	6 W178V	8 W178G	11 W178F	5 W178M
F	7	6 W178Y	6 W178S	5 W178A	8	11 W178V	10 W178F	11 W178H	5 W178M	8 W178W	8 W178W	21 W178Q
G	7 W178Y	4 W178I	9 W178S	6 W178V	10 W178W	11 W178S	21 W178E	0 W178P	14 W178S	12 W178G	12 W178L	4 W178I
H	19 W178N	13 W178Q	7 W178S	9 W178C	10 W178W	5 W178I	6 W178F	0 No data	5 W178T	8 W178V	10 W178H	Control

B Ace W178X on Ace-mNeon2 S81D D92N R78K (well B10 from above)

	1	2	3	4	5	6	7	8	9	10	11	12
A	40 W178Y	11 W178Q	8 W178N	15 W178C	40 W178L	38 W178W	8 W178S	40 W178W	0 No data	31 W178C	32 W178V	16 W178N
B	39 W178Y	27 W178K	18 W178N	39 W178Y	35 W178Y	24 W178K	32 W178I	23 W178G	40 W178Y	28 W178T	42 W178W	25 W178C
C	0 W178R	0 W178P	25 W178H	35 W178V	46 W178F	25 W178G	30 W178M	42 W178W	36 W178Y	41 W178W	37 W178W	25 W178C
D	40 W178W	26 W178I	43 W178T	38 W178W	45 W178F	12 W178D	21 W178P	34 W178V	31 W178T	40 W178V	46 W178C	Control

Figure S8 | High-throughput screening for voltage sensitivity of positive-polarity variant Ace-mNeon2 S81D D92N.
(A) 48 variants containing saturation mutations at Ace R78 or W178 on the backbone of Ace-mNeon2 S81D D92N were each transfected in electrically excitable HEK cells (*30,31*) and screened for voltage sensitivity on the high-throughput platform (*18*). The maximum %$\Delta F/F$ obtained for each variant across 4 independent rounds of screening are indicated in each well together with the sequence information. Color density corresponds to the size of the signal in the positive direction.
(B) Same as above for Ace W178X mutagenesis on Ace-mNeon2 S81D D92N R78K backbone.

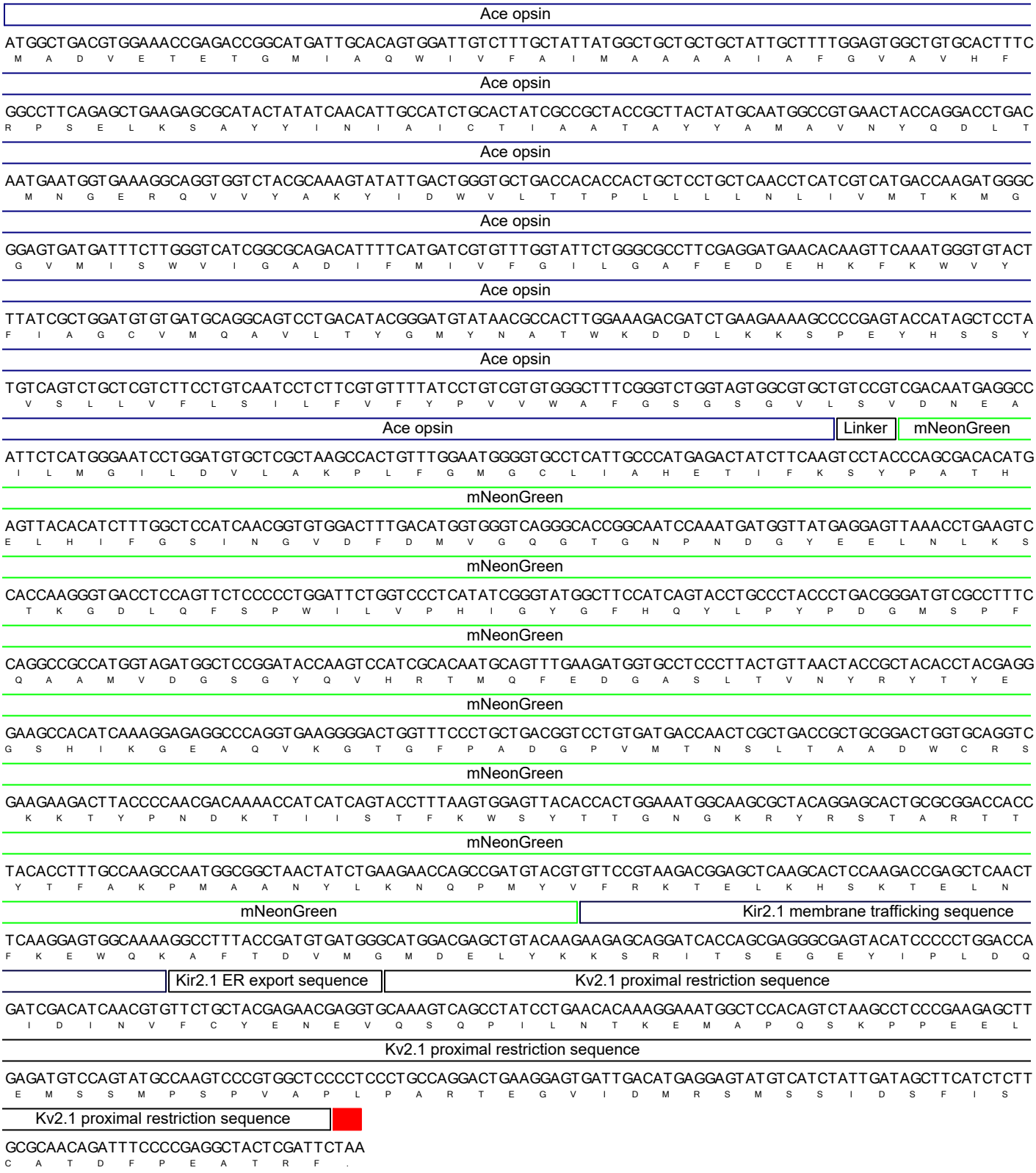

Figure S9 | DNA and amino acid sequences of PACE fused to a somatic restriction sequence from Kv2.1.

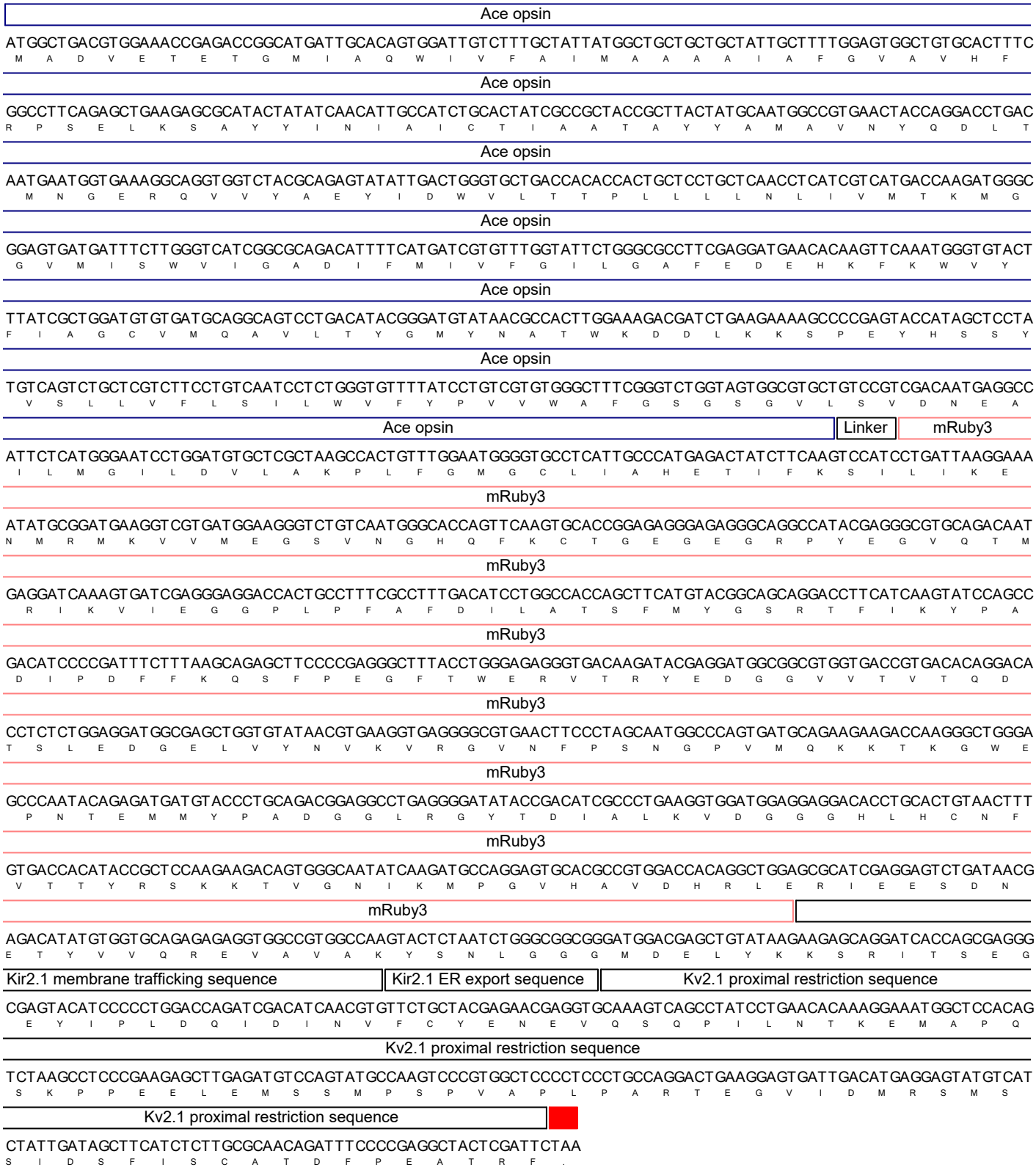

Figure S10 | DNA and amino acid sequences of PACER fused to a somatic restriction sequence from Kv2.1.

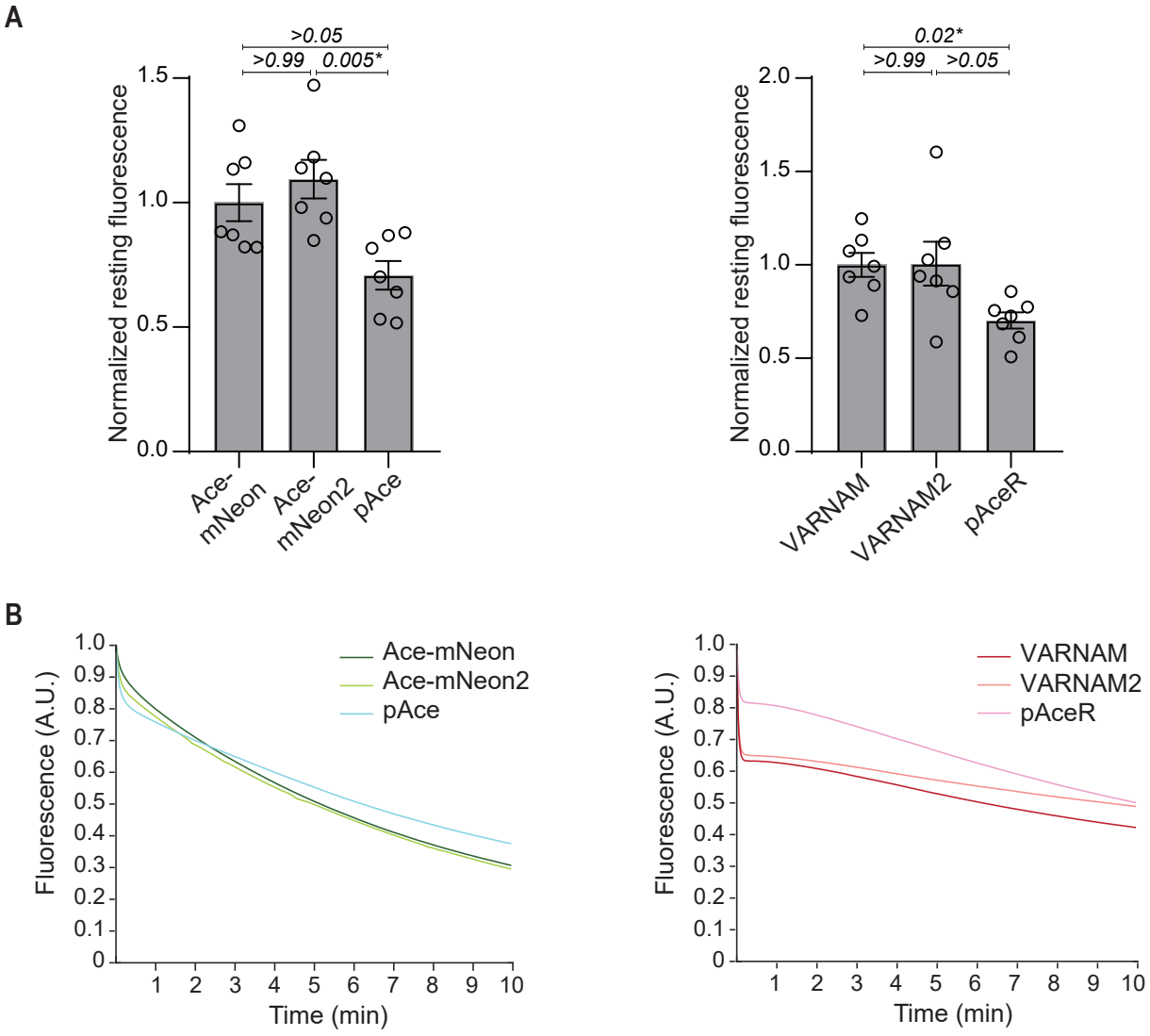

Figure S11 | Brightness and photobleaching characteristics of the FRET-opsin indicators.
(A) *Left*, Resting fluorescence of Ace-mNeon, Ace-mNeon2 and pAce normalized to average resting intensity of Ace-mNeon. Values represent mean ± S.E.M. P values are italicized. Statistical comparisons were made across all conditions. Asterisks denote significance (Kruskal-Wallis test with Dunn's multiple comparisons correction). *Right*, same as above for VARNAM, VARNAM2 and pAceR (n=7 wells/condition, ~500 cells/well).
(B) Photobleaching profiles of Ace-mNeon, Ace-mNeon2 and pAce (*left*) and VARNAM, VARNAM2 and pAceR (*right*) in HEK cells under continuous illumination (n=4 wells each, ~100 cells/well) Imaging conditions: 505 nm LED for the green indicators and 565 nm LED for the red indicators, 25 mW mm^{-2} at sample plane.

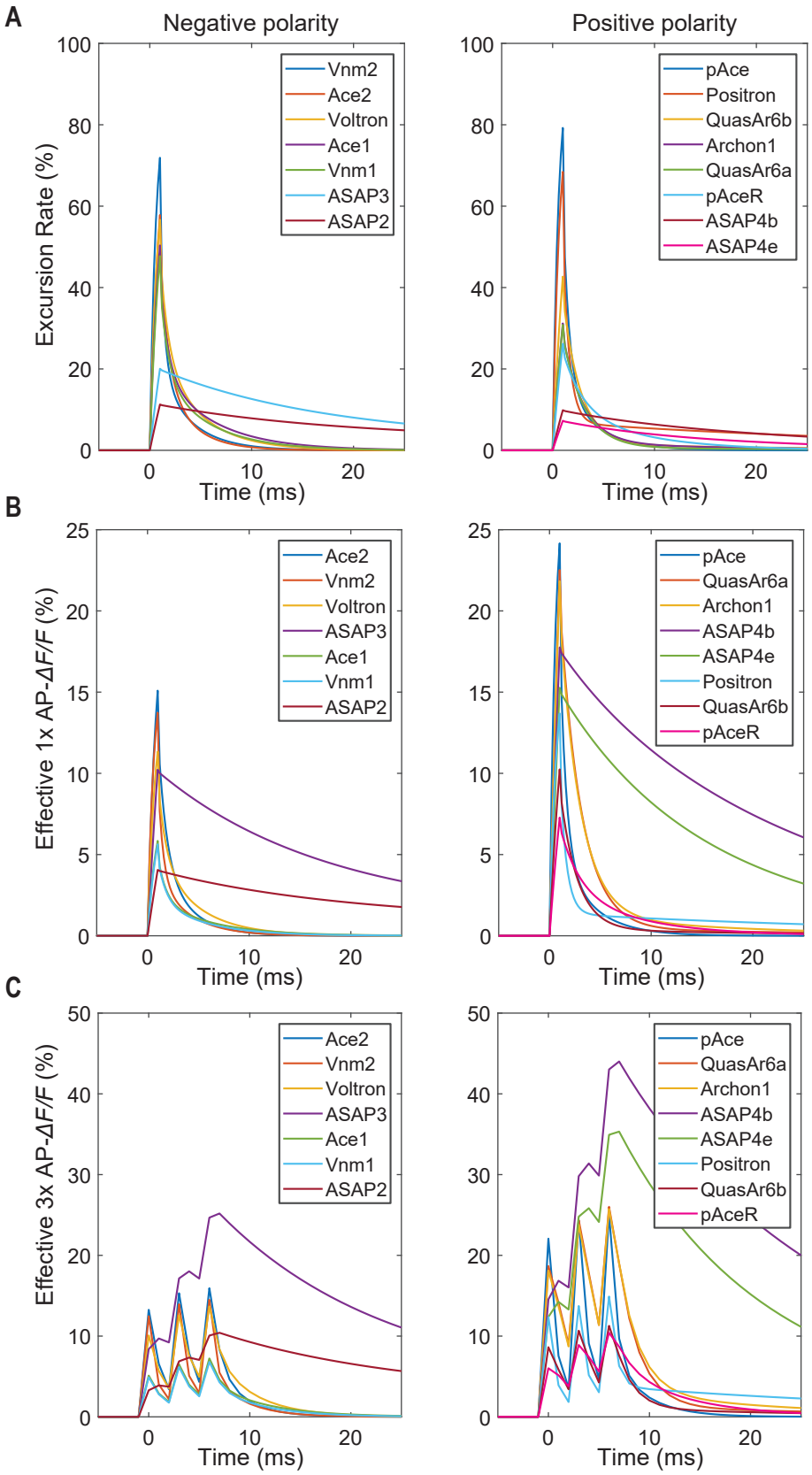

Figure S12 | Benchmarking GEVIs based on their 1 ms impulse responses calculated using reported values of intrinsic response kinetics (see Methods).
(A) Excursion rate, defined as the effective amplitude of the saturated *ΔF/F*, for negative and positive polarity GEVIs. GEVIs are ranked in decreasing order of peak saturated *ΔF/F*. Sampling rate: 5 kHz.
(B) Effective *ΔF/F* for 1x AP. Sampling rate: 5 kHz.
(C) Effective *ΔF/F* for 3x AP spike burst, 3 ms refractory period. Sampling rate: 1 kHz.

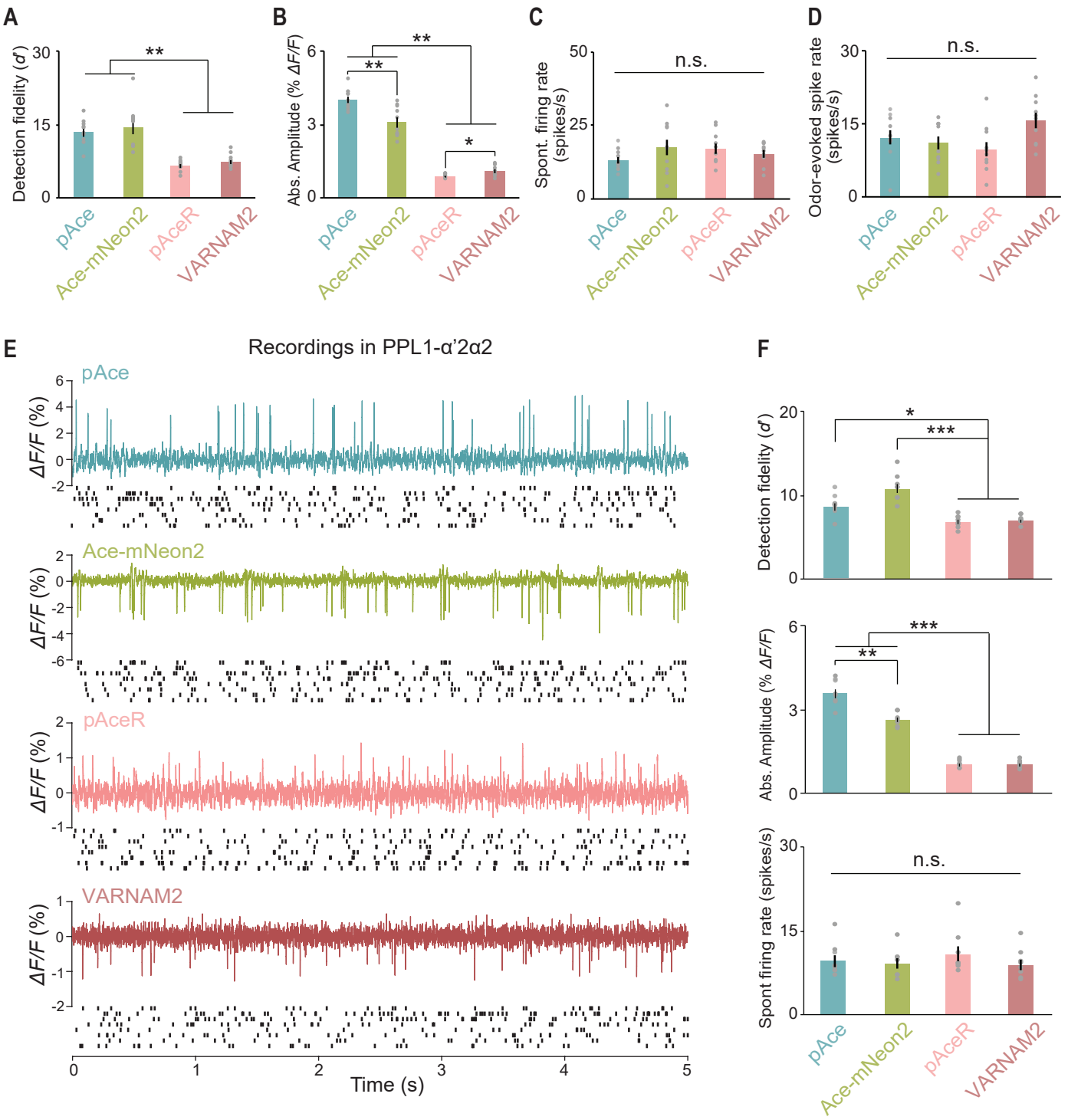

Figure S13 | Characterization of the FRET-opsin indicators in PPL1-γ2α'1 and PPL1-α'2α2 neurons in *Drosophila*.
(A-D) Comparisons of (A) spike detection fidelities (B) absolute amplitudes (C) mean spontaneous firing rates, and (D) odor-evoked firing rate change obtained from recordings in PPL1-γ2α'1 expressing each of the four indicators. (n = 10 trials; 2 trials per fly; **P*<0.05, ***P*<0.01, ****P*<0.001, n.s.=not significant, Kruskal-Wallis ANOVA and post-hoc Mann-Whitney U-tests with Holm-Bonferroni correction).
(E) Representative optical recordings (*top*) and raster plots (*bottom*) of 5-s spontaneous spiking in a PPL1-α'2α2 neuron expressing pAce, Ace-mNeon2, pAceR or VARNAM2 (n = 8 trials; 2 trials per fly).
(F) Comparisons of detection fidelities (*top*), absolute amplitudes (*center*), and mean spontaneous firing rates (*bottom*) in PPL1-α'2α2 neurons. (n = 8 trials; 2 trials per fly; **P*<0.05, ***P*<0.01, ****P*<0.001, Kruskal-Wallis ANOVA and post-hoc Mann-Whitney U-tests with Holm-Bonferroni correction).

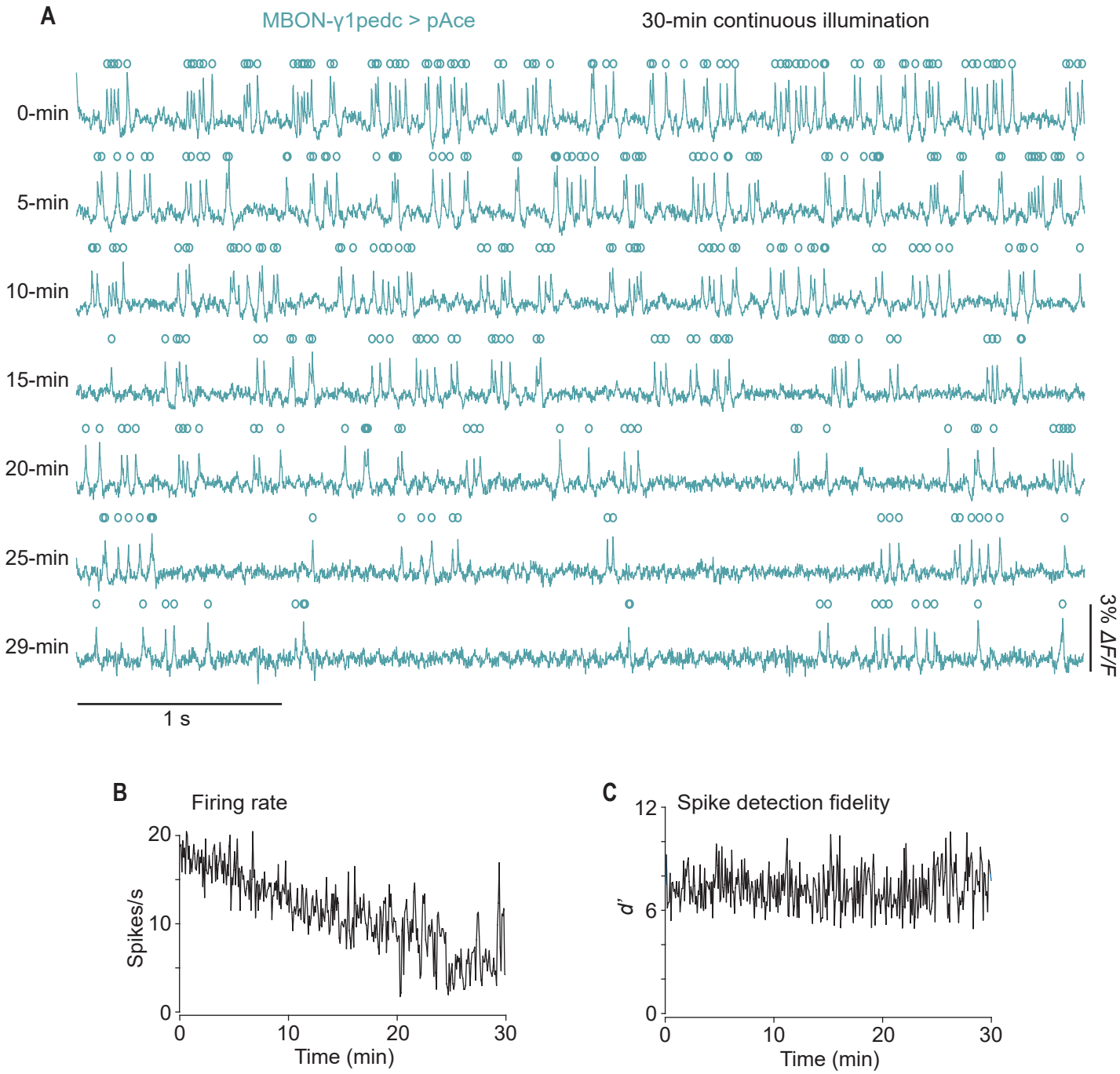

Figure S14 | 30-min continuous imaging using pAce in *Drosophila*.
(A) Example 5 s recordings collected at regular time intervals during 30-min continuous illumination showing spontaneous spiking in a MBON-γ1pedc>α/β neuron expressing pAce.
(B) Time-varying spike rate in the recorded MBON-γ1pedc>α/β neuron during the 30-min imaging session.
(C) Spike detection fidelity in the recorded MBON-γ1pedc>α/β neuron during the 30-min imaging session.

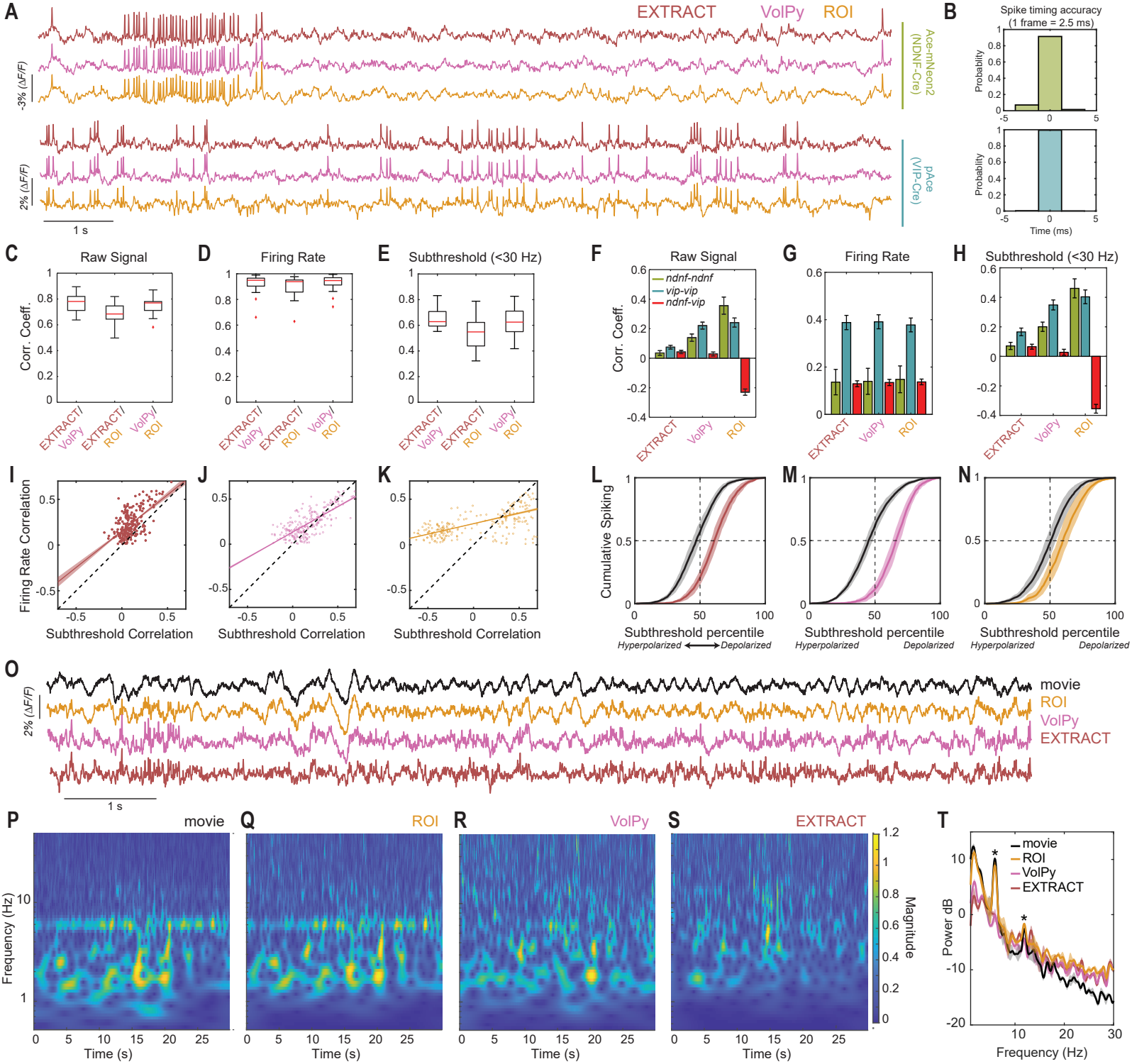

Figure S15 | Benchmarking of VolPy and EXTRACT algorithms against ROI-based cell segmentation.
(A): Example time-traces estimated using ROI segmentation (yellow), VolPy (purple), or EXTRACT (red) for NDNF- and VIP-neurons labelled with Ace-mNeon2 or pAce, respectively (data from Fig. 3C). Note the excess spiking cross-talk on the ROI traces. (B): Spike timing accuracy between spikes detected on EXTRACT versus VolPy traces. (C-E): Box plots of cross-correlation coefficients between each pair of extraction methods for (C) raw signals, (D) firing rate signals, and (E) subthreshold signals. (F-H): Pairwise correlation coefficients within and between NDNF/VIP populations, across all three extraction methods for (F) raw signals, (G) firing rate signals, and (H) subthreshold signals. Note that all three methods provide identical firing rate correlations whereas the ROI-method strongly overestimates subthreshold cross-correlation, likely due to excess hemodynamic artifacts. Data represented as mean ± 95% CI. (I-K): Effect of the subthreshold input dynamics on the spiking output dynamics between pairs of neurons, whose time-traces are estimated using (I) EXTRACT, (J) VolPy, or (K) ROI. Circles represent each pair of neurons. The dash line is the first bisector. Note that pairs of neurons with shared subthreshold synaptic inputs tend to fire together. (L-N): (L) EXTRACT, (M) VolPy, or (N) ROI captures the increased spiking likelihood during subthreshold depolarization (Data: mean ± 99% CI). (O): Time-series corresponding to temporal averaging of the processed movie pixels (black) and temporal averaging of all neurons' time traces estimated by each extraction method. (P-S): Wavelet spectrograms of every time series in (D), showing strong spectral content overlap between (P) movie average and (Q) ROI but not with (R) VolPy or (S) EXTRACT. (T): Power spectrum density of (D), showing that VolPy and EXTRACT, but not ROI-based, are immune to correlated background fluctuations (*: heartbeat fundamental frequency at ~6 Hz and its first harmonics ~12 Hz).

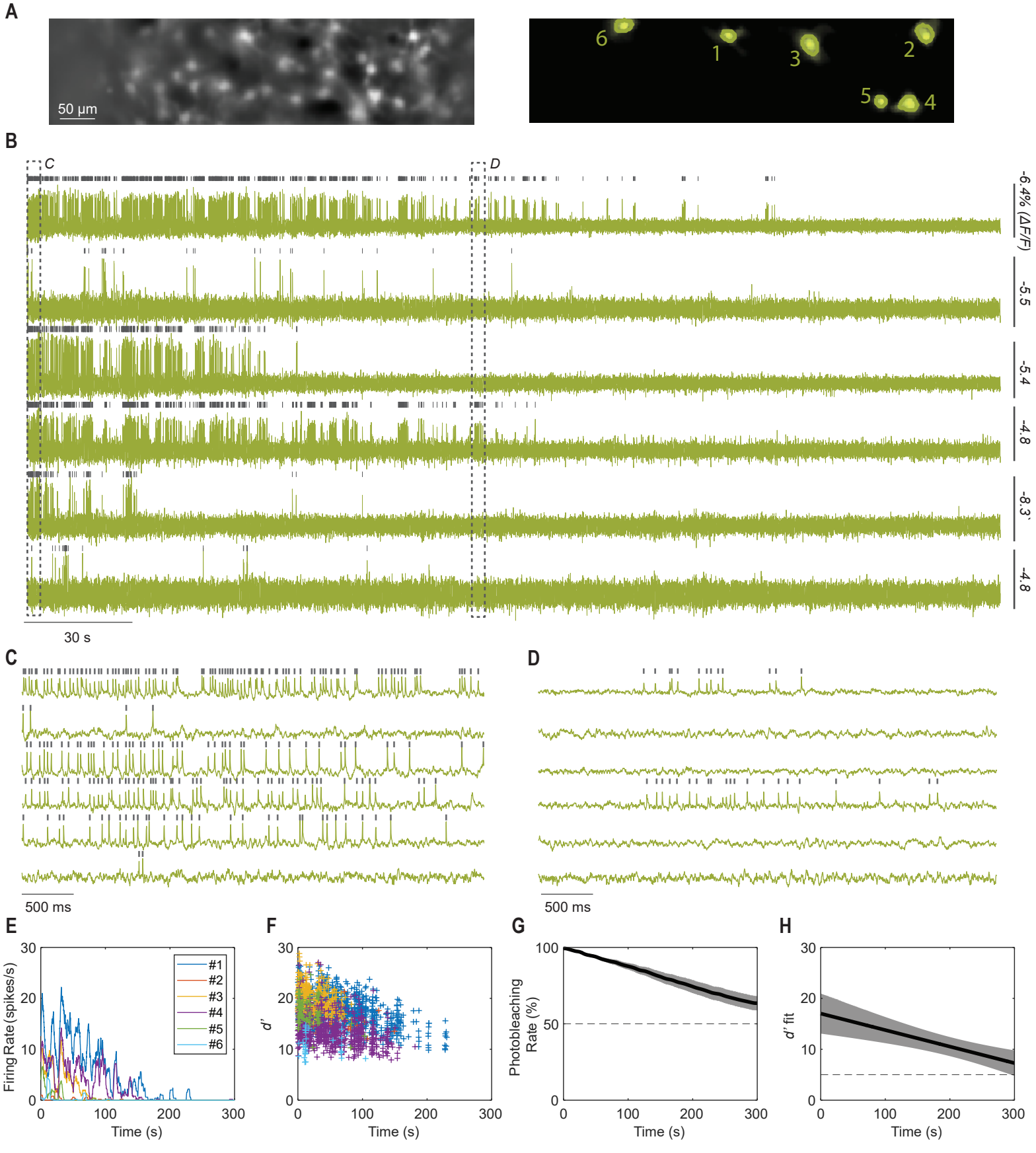

Figure S16 | 5 min-long *in vivo* spike imaging using Ace-mNeon2 in awake mouse.
(A) *Left,* Representative raw epifluorescence image and *right,* spatial footprints of Ace-mNeon2 signals from 6 identified V1 NDNF interneurons.
(B-D) *ΔF/F* traces for all neurons in (A). Dashed boxes are expanded in (C-D).
(E) Time course of firing rate for all neurons in (B).
(F) Time course of spike detection metric *d'* for all neurons in (B).
(G) Average photobleaching rate across all neurons in (B).
(H) Average of the *d'* values for all neurons in (F).

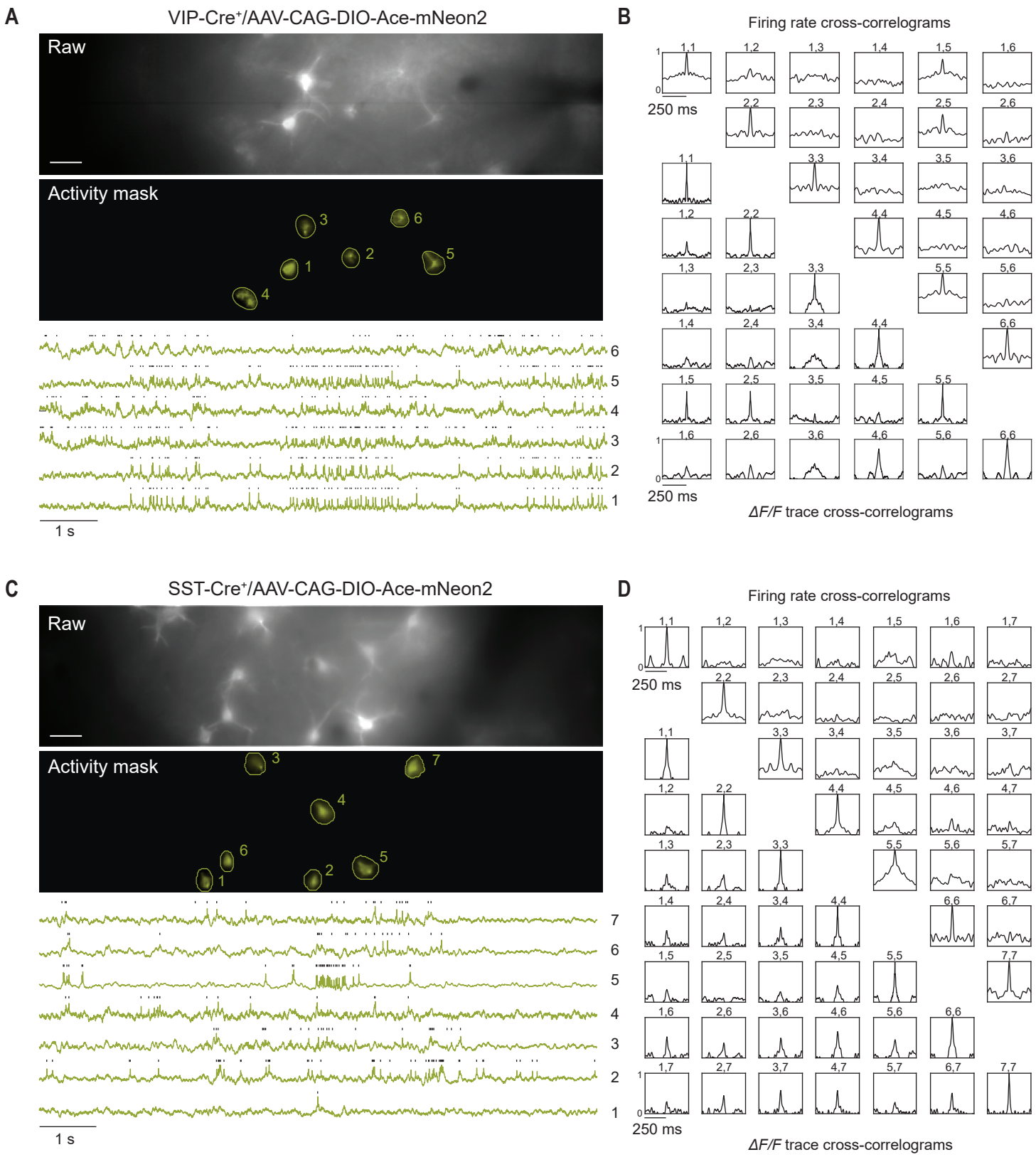
A
VIP-Cre+/AAV-CAG-DIO-Ace-mNeon2
Raw
Activity mask
1 s
B
Firing rate cross-correlograms
250 ms
ΔF/F trace cross-correlograms
C
SST-Cre+/AAV-CAG-DIO-Ace-mNeon2
Raw
Activity mask
1 s
D
Firing rate cross-correlograms
250 ms
ΔF/F trace cross-correlograms

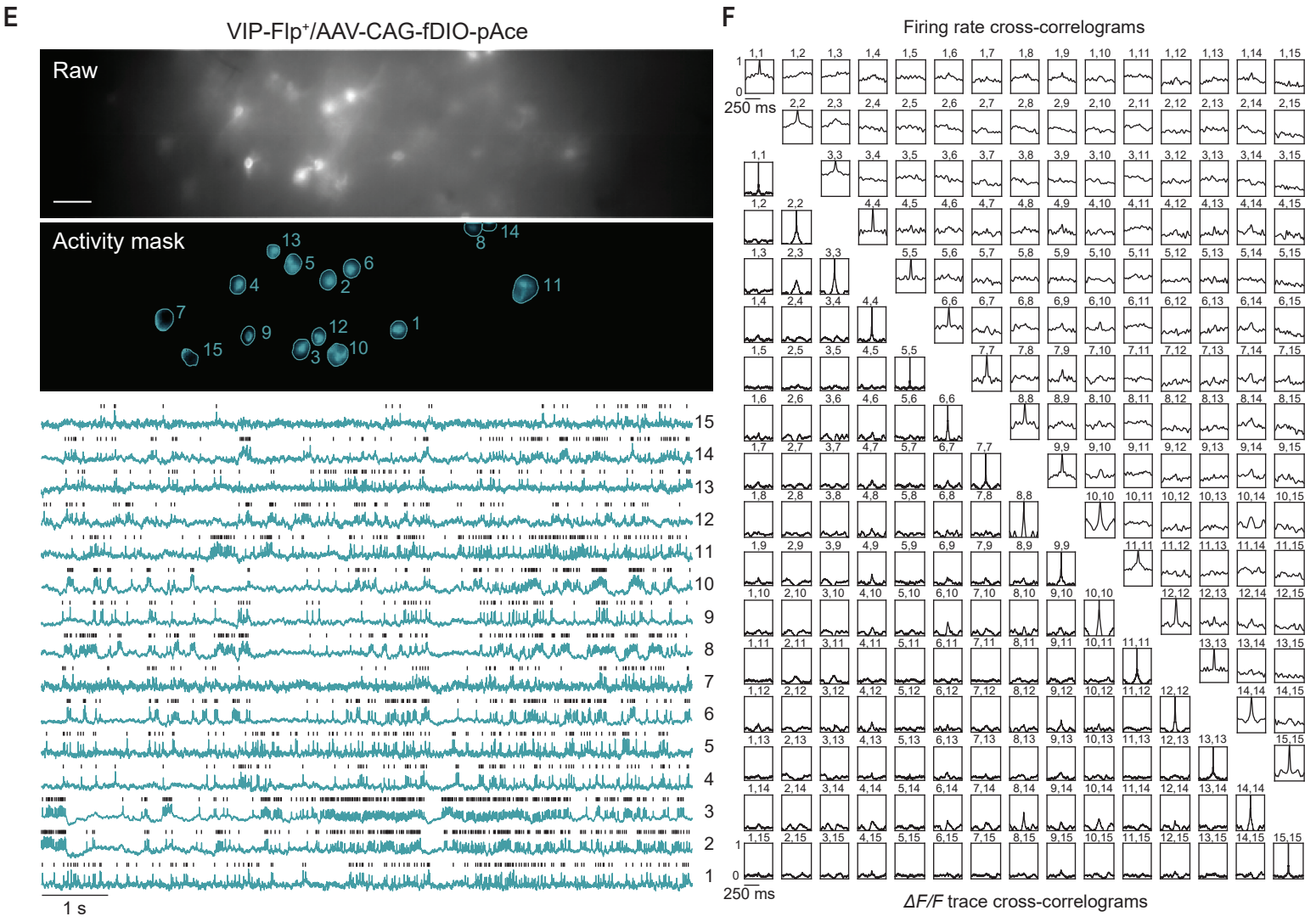

Figure S17 | Minimal cross-contamination of voltage signals from adjacent cells in widefield recordings.
(A) *Top,* Representative epifluorescence image of a single field-of-view from a VIP-*Cre*$^+$ mouse, expressing *Cre*-dependent soma-targeted Ace-mNeon2 in V1. Scale bar: 50 µm. *Center,* mask image showing active ROIs. *Bottom, ΔF/F* traces showing spontaneous activity from the ROIs numbered in the mask image.
(B) Auto- and cross-correlograms of *top,* the firing rates with a sliding window of 20 ms and *bottom,* the *ΔF/F* traces for neuron-pairs in the field-of-view above.
(C) Same as (A) for recordings from an SST-*Cre*$^+$ mouse.
(D) Same as (B) for the field-of-view in (C).
(E) Same as (A) for recordings from a VIP-*Flp*$^+$ mouse, expressing *Flp*-dependent soma-targeted pAce in V1.
(F) Same as (B) for the field-of-view in (E).

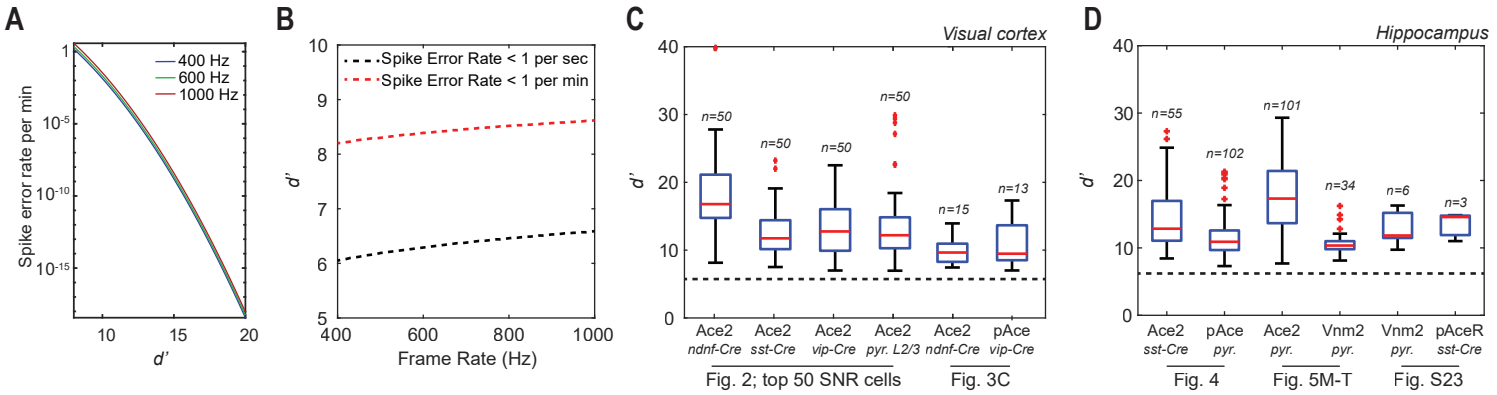

Figure S18 | Spike detection fidelity index *d'* estimated for the four GEVIs expressed in various hippocampal and cortical cell-types.
(A) Spike detection error rate as a function of *d'* for the three different imaging frame rates used in this study (see Materials and methods and Wilt *et al.*, 2013 (*38*)).
(B) Minimum *d'* values required to reach a given spike detection error rate as a function of the imaging frame rate.
(C-D) Box plot of *d'* values for different datasets acquired in (B) visual cortex and (C) hippocampus. The indicator, cell-type, and associated main figure panel/s are indicated on the x-axis. For each box plot, the central red line, bottom, and top edges indicate the median, 25th, and 75th percentile values, respectively. Outliers '+' are values beyond 1.5 times the interquartile range from the top or bottom edge of the box. The whiskers extend to the data points not considered outliers.

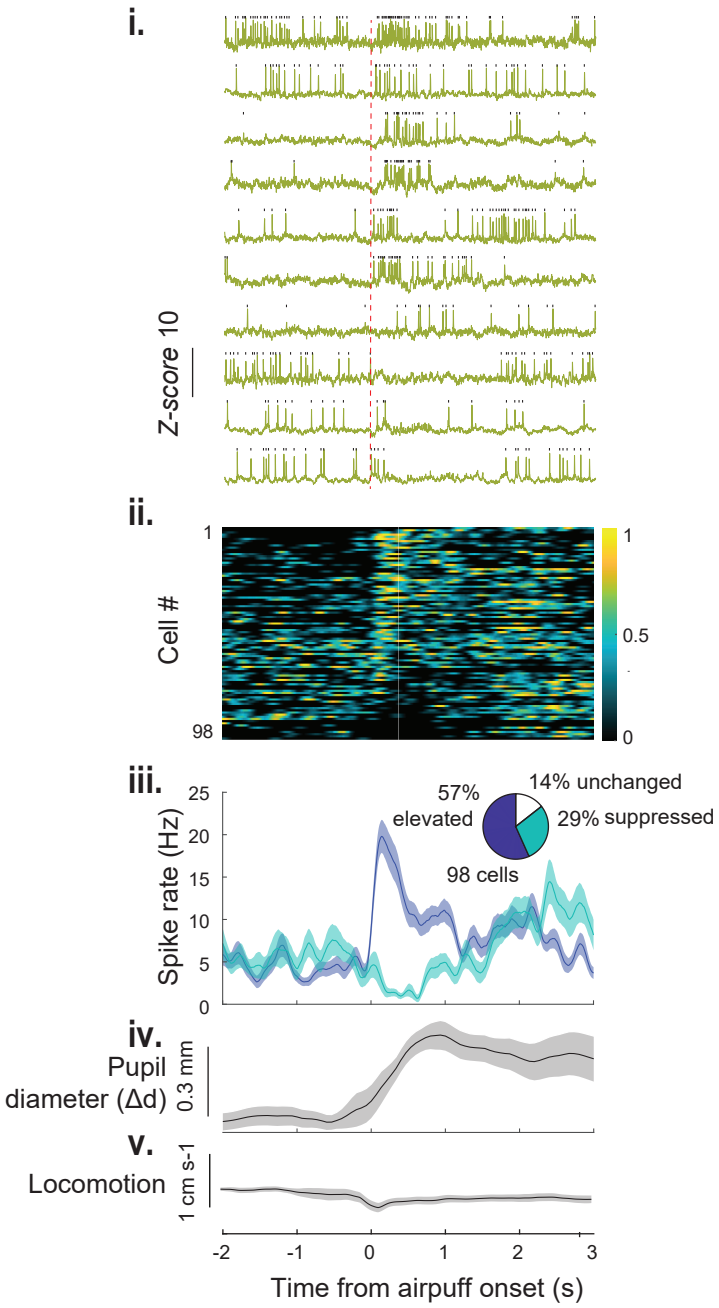

Figure S19 | Effects of arousal without locomotion on VIP-interneuron firing rates.
(i) Example fluorescence-time traces from individual VIP-interneurons. Vertical dashed line indicates air puff onset. Grey ticks denote identified spikes. (ii) Z-scored firing rate PSTH for all VIP-interneurons (n=98 cells, 8 mice). Cells are arranged in order of decreasing spike modulation indices (see Methods). (iii) Mean ± S.E.M. firing rate aligned to air puff onset for activated (dark blue) and suppressed (cyan) fractions. Pie chart inset indicates % cells with elevated (dark blue), suppressed (cyan), or unchanged (white) spike rates following air puff. (iv) Mean ± S.E.M. change in pupil diameter for all trials.
(v) Mean ± S.E.M. locomotory speed for all trials.

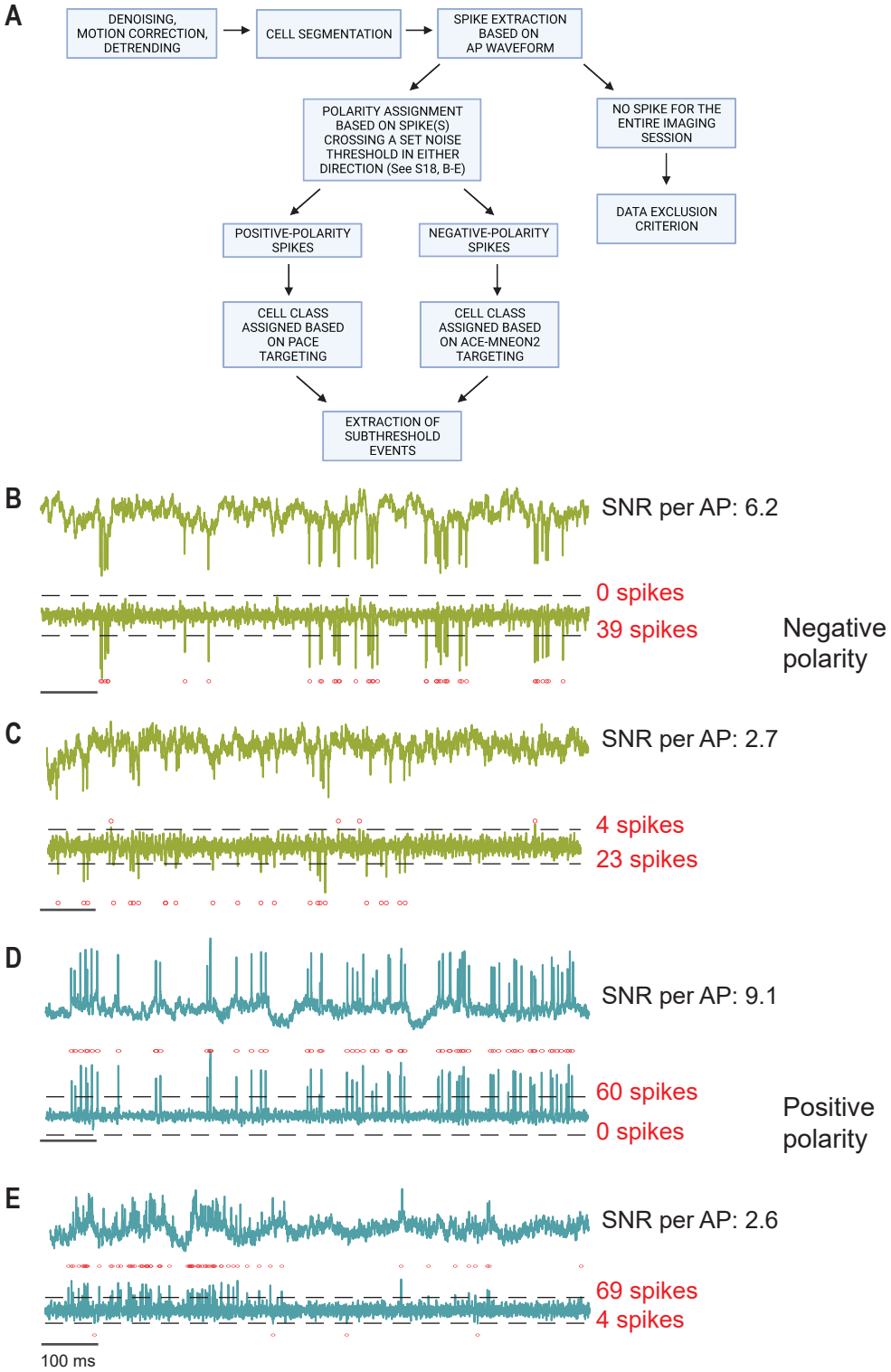

Figure S20 | Polarity assignment in V1 DUPLEX recordings in awake mice (see also Methods).
(A) Schematic of the automated data analyses pipeline with integrated cell sorting. Briefly, all fluorescent cells are identified and fed into the spike extraction algorithm, which identifies spikes based on AP waveform characteristics. Trials with no APs meet the data exclusion criterion and are removed from further analyses. Cell-class identity is established based on whether the identified spikes are of positive or negative polarity (see B-E). Subthreshold events for data curation are extracted after cell-class is determined.
(B) *Top*, representative raw and, *bottom*, spike-identified $\Delta F/F$ traces from a cell exhibiting negative-polarity spikes at high SNR. Dashed lines indicate 3x S.D. of baseline in either direction. Transients that surpassed this threshold were identified as spikes (red circles) and the direction with the most number of spikes determined the spike polarity. Thus, this neuron was assigned a negative-polarity and the neuron-type was inferred based on Ace-mNeon2 targeting.
(C) Same as (B) for a low SNR trace.
(D) *Top*, representative raw and, *bottom*, spike-identified $\Delta F/F$ traces from a cell exhibiting positive-polarity spikes at high SNR. Dashed lines indicate 3x S.D. of baseline in either direction. Transients that surpassed this threshold were identified as spikes (red circles) and the direction with the most number of spikes determined the spike polarity. Thus, this neuron was assigned a positive-polarity and the neuron-type was inferred based on pAce targeting.
(E) Same as (D) for a low SNR trace.

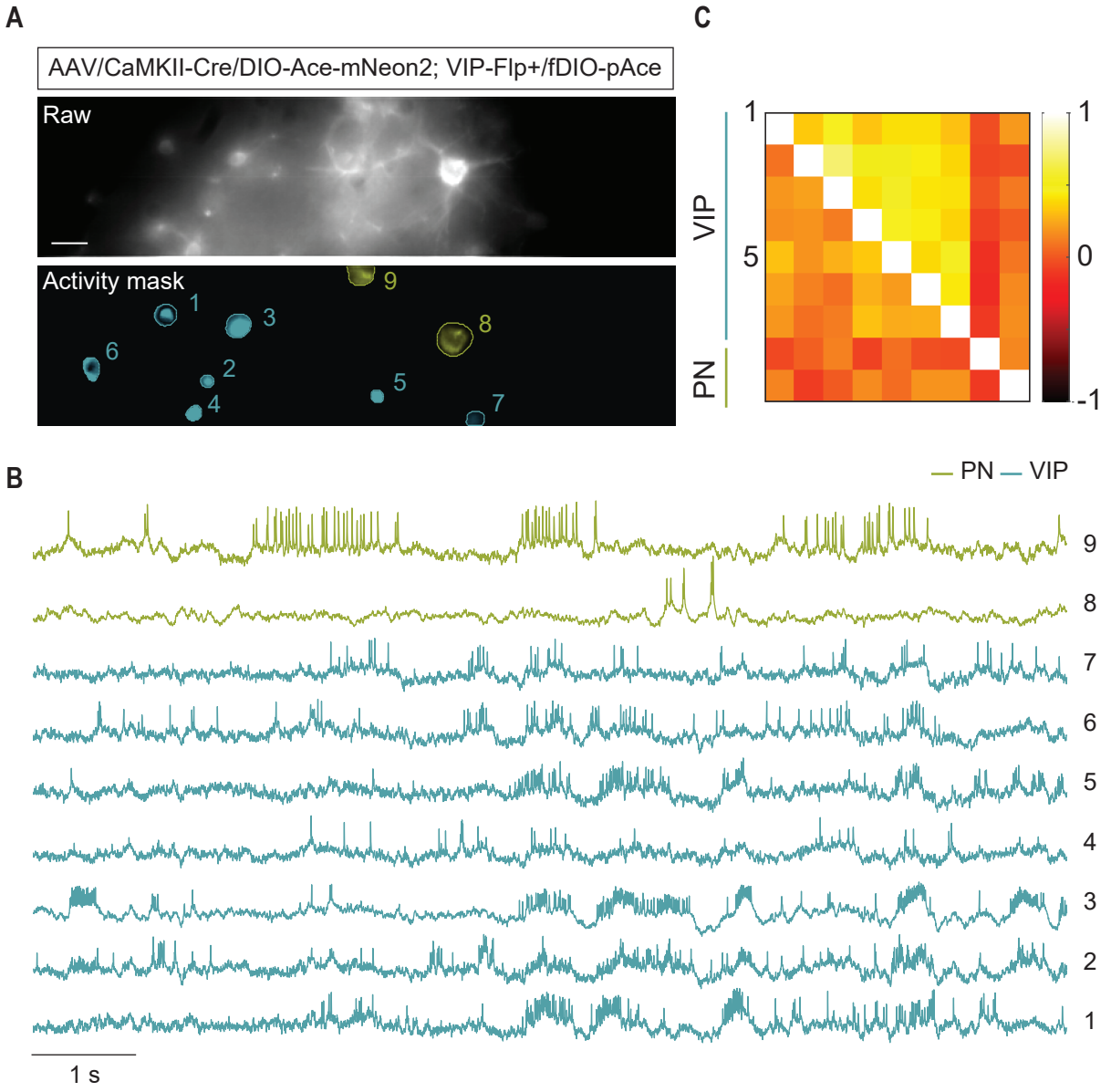

Figure S21 | Example DUPLEX recordings from PNs and VIP-interneurons.
(A) Raw epifluorescence (*top*) and activity-mask (*bottom*) images of a single field-of-view from a a VIP-*Flp*$^{+}$ mouse expressing Ace-mNeon2 in PNs (green) and pAce in VIP-interneurons (blue). Active regions-of-interest (ROIs) are numbered. Scale bar: 50 μm.
(B) $\Delta F/F$ traces from the ROIs numbered in (A). Ace-mNeon2 traces are inverted for visualization purposes.
(C) Intra- and inter-population correlation coefficient matrix constructed from pairwise, zero time-lag correlation coefficients of the $\Delta F/F$ traces in (B).

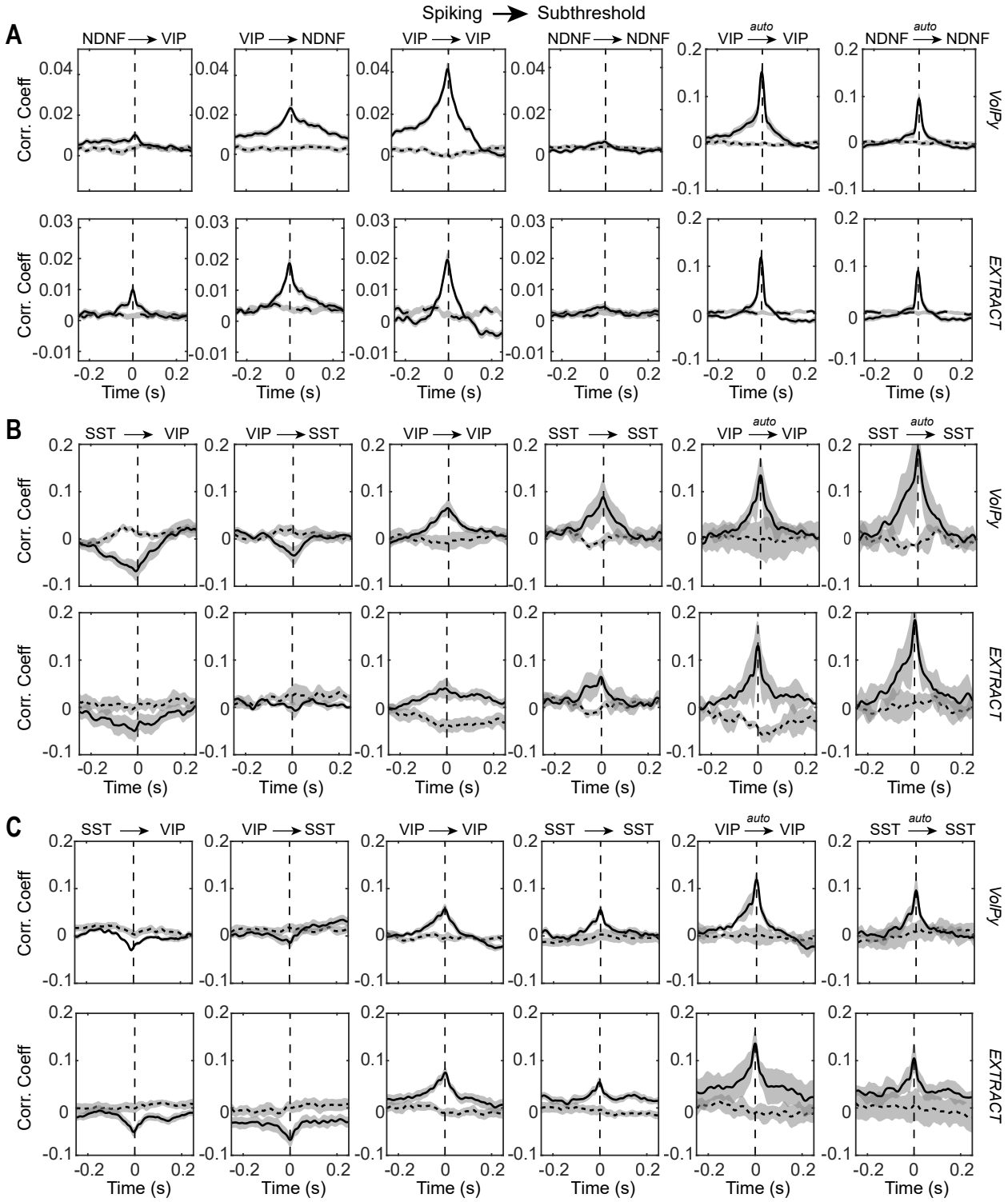

Figure S22 | Spiking and subthreshold cross-correlations within and between cell-types in DUPLEX recordings during spontaneous behavior.

(A) NDNF/VIP DUPLEX recording (from Fig. 3, C-D) (n=13 NDNF neurons, n=15 VIP neurons).

(B) SST/VIP DUPLEX recording (from Fig. 3, E-F) (n=3 SST neurons, n=4 VIP neurons).

(C) Additional field-of-view of SST/VIP DUPLEX recording (n=5 SST neurons, n=5 VIP neurons).

Solid plots represent cross- or auto-correlograms. Dotted plots represent shuffled correlograms, obtained from random circular permutations of spike trains. The first 2 columns are cross-correlograms of spiking in one with the subthreshold activity in another class, the central 2 columns are cross-correlograms of spiking with subthreshold within the same class but across distinct neurons, and the last 2 columns are auto-correlograms for the same neurons. All results are qualitatively identical whether VolPy or EXTRACT algorithms were used for automatic cell segmentation. The anti-correlation between spiking and subthreshold dynamics is only observed between SST and VIP. This anticorrelation is likely a bona fide phenomenon, by which the firing pattern in one cell-type predicts the subthreshold activity in another cell-type. Indeed, a DUPLEX-related artifact should equally affect all DUPLEX recordings, irrespective of cell-types, which is not the case for NDNF/VIP recordings. Note that the VIP plots are consistent across (A-C), and that the last two columns are reminiscent of Fig. S15, L-N, showing that spiking occurs during a depolarized state.

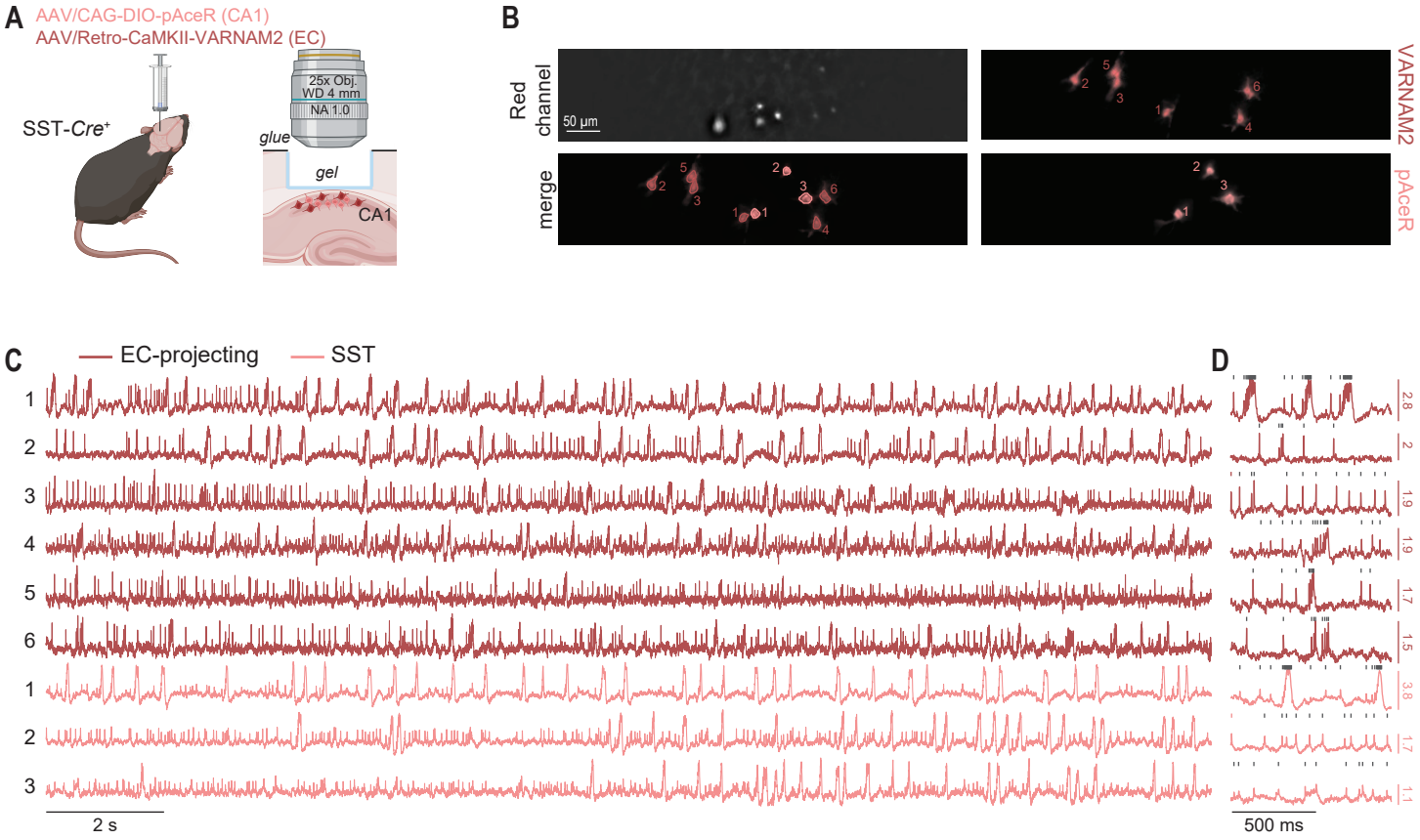

Figure S23 | Red-DUPLEX reports the simultaneous voltage dynamics from two genetically identified neuron classes in hippocampus of awake mice.
(A) Schematic of AAV injections and experimental setup for red-DUPLEX using VARNAM2 and pAceR.
(B) Representative raw epifluorescence image and spatial footprints of negative- and positive-polarity signals (in dark red and pink, respectively) of 6 and 3 identified neurons. Scale bar: 50 µm.
(C) *ΔF/F* traces for all neurons in (B), representing CA1 EC-projecting excitatory neurons, and local SST-interneurons expressing VARNAM2 and pAceR, respectively. VARNAM2 traces are inverted for visualization purposes.
(D) First 1 s of (C), with the location of detected spikes. The scale bars to the right indicate peak-to-peak *ΔF/F*(%).

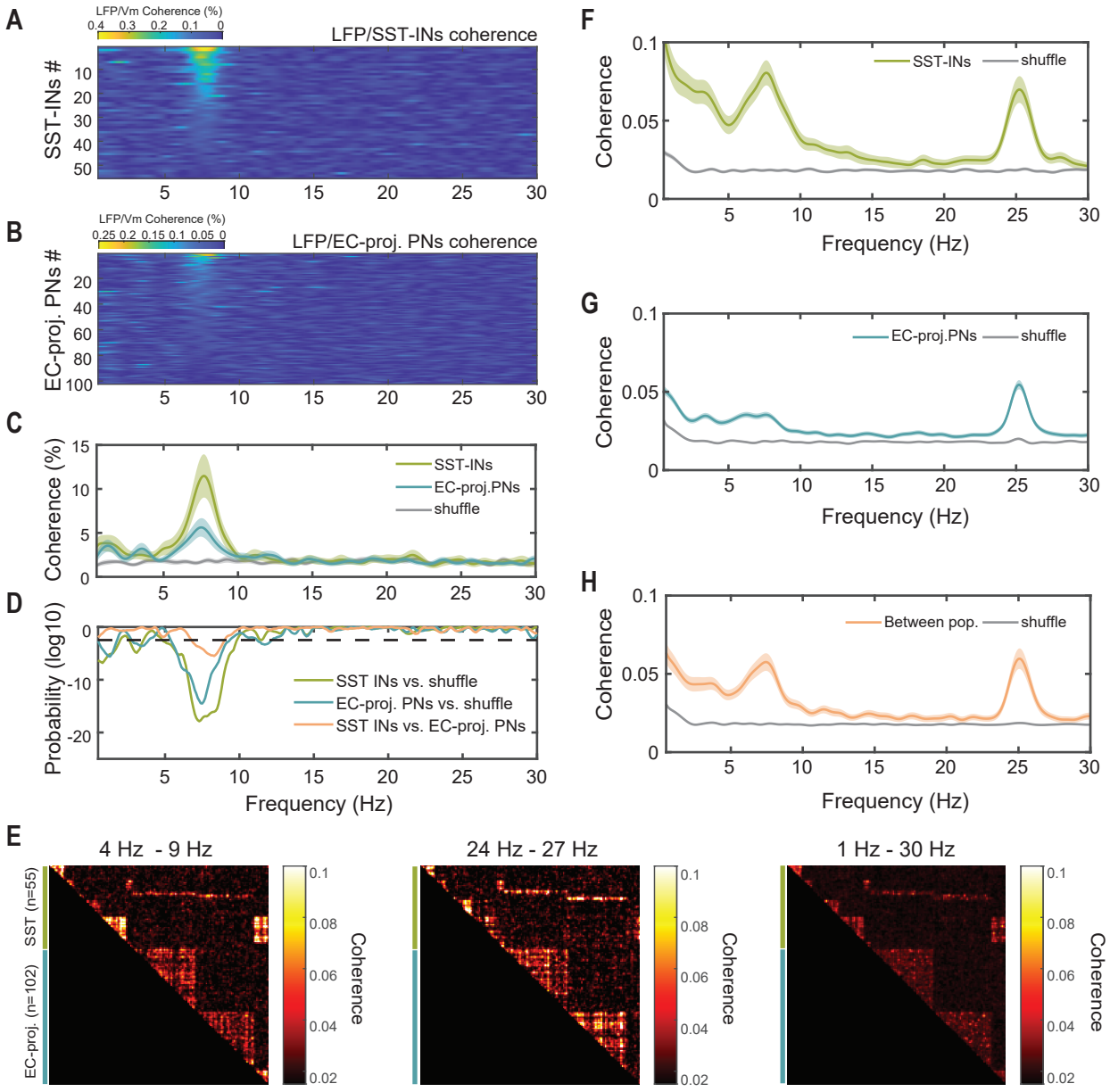

Figure S24 | Subthreshold contributions of excitatory versus inhibitory neuronal populations to the local field potentials and pairwise coherence of excitatory/inhibitory neuronal ensembles.
(A-D) Subthreshold analysis of excitatory versus inhibitory contributions to local field potentials.
(A) LFP coherence raster plot for all SST-interneurons (n=55 cells, 6 fields-of-view, 1 mouse), sorted by theta-band coherence strength.
(B) LFP coherence raster plot for all EC-projecting PNs (n=102 cells, 6 fields-of-view, 1 mouse), sorted by theta-band coherence strength.
(C) LFP coherence averages across all neurons in (A-B). Shaded area: 95% CI.
(D) Pairwise probability of data from (C), assessed at each frequency point using Wilcoxon rank sum test. The dashed line corresponds to Bonferroni-corrected significance threshold (P <0.01).
(E-H) Frequency-averaged coherence between excitatory/inhibitory neuronal ensembles.
(E) Pairwise coherence matrices averaged over narrow band theta (4-9 Hz, *left*), beta (24-27 Hz, *center*), or broad band frequencies (1-30 Hz, *right*). Note that the off-diagonal hot-spot patches represent neuronal ensembles belonging to the same fields-of-view.
(F-H) Population-averaged pairwise coherence plots computed for (F) SST-neuronal ensembles, (G) EC-projecting PN ensembles, and (H) between SST-interneurons and EC-projecting PNs. Note that neuronal ensembles are more strongly correlated in the theta and beta frequencies, suggesting shared synaptic inputs at those frequencies. Shuffle traces are estimated from neurons belonging to different fields-of-view. Shaded area: 95% CI.

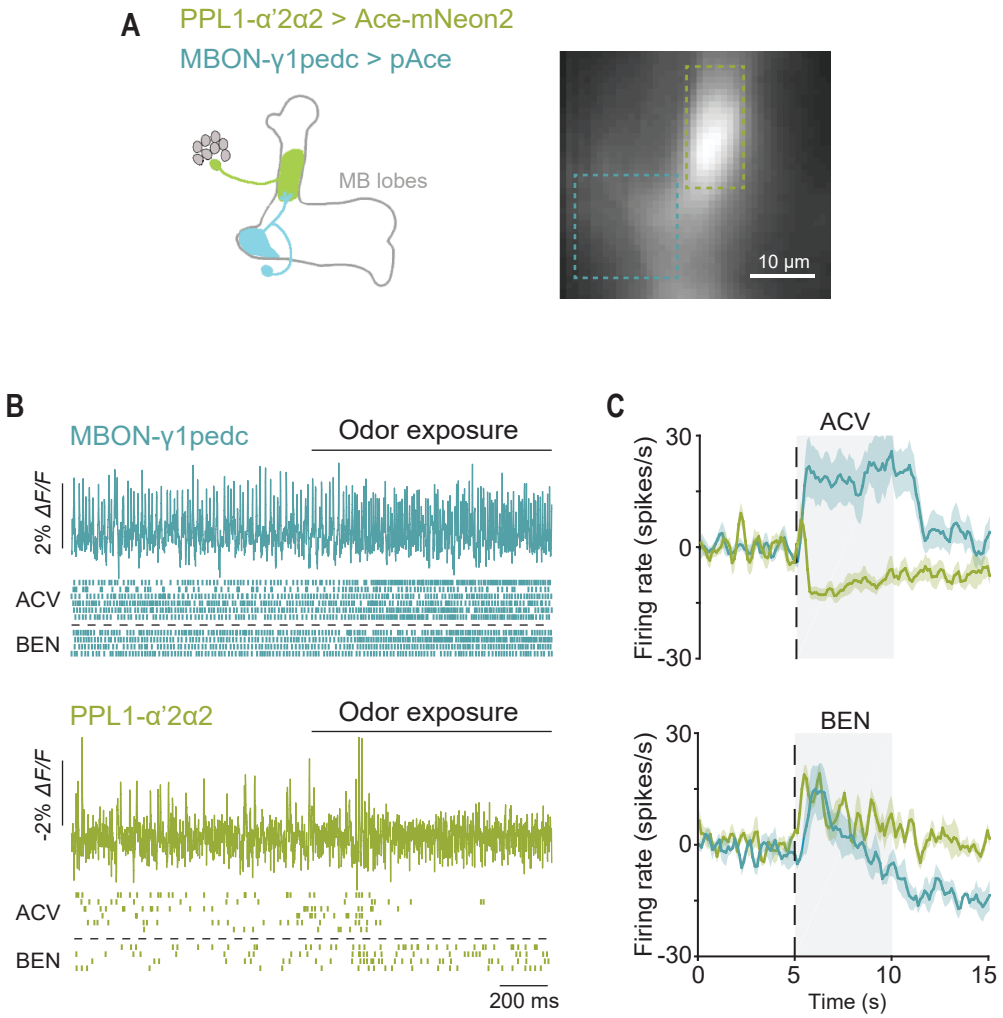

Figure S25 | Dual-polarity voltage imaging in flies.
(A) *Left*, Cartoon and *right*, epifluorescence image showing expression of Ace-mNeon2 and pAce in two synaptically connected neuron-types for simultaneous dual-polarity voltage imaging. Dashed boxes indicate regions-of-interest comprising the axonal region of PPL1-α'2α2 neuron (*green*, Ace-mNeon2) and the dendritic region of MBON-γ1pedc >α/β neuron (*blue*, pAce).
(B) Example traces of evoked spiking during a 2 s time-window around odor onset from a 15-s imaging trial. Raster plots showing responses during 6 trials of exposure to the attractive odorant apple cider vinegar (ACV) and 4 trials of exposure to the repulsive odorant benzaldehyde (BEN) obtained from PPL1-α'2α2 and MBON-γ1pedc>α/β neurons.
(C) Mean spike rate change during ACV (*top*) and BEN (*bottom*) exposure in in the two neurons. (n = 6 trials for ACV; n = 4 trials for BEN; 2 trials per fly).

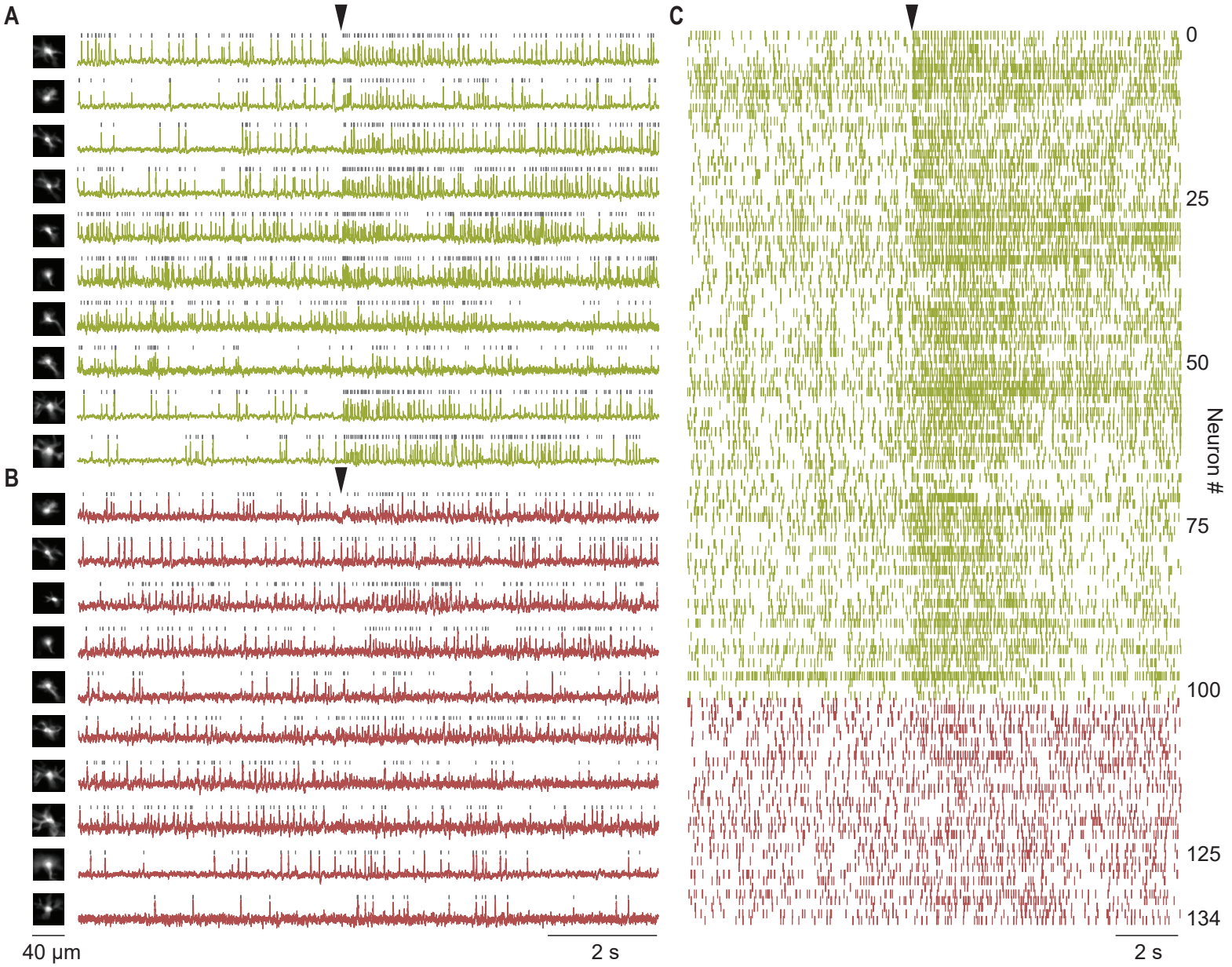

Figure S26 | Voltage recordings from ACC- and EC-projecting excitatory neurons in dorsal CA1 in an awake behaving mouse during behavioral state transition.
(A) Example Δ*F/F* traces from ACC-projecting PNs retrogradely labeled with Ace-mNeon2.
(B) Example Δ*F/F* traces from EC-projecting PNs retrogradely labelled with VARNAM2.
(C) Summary raster plot for all 134 projection neurons (n=5 fields-of-view, 1 mouse). Arrows indicate rest-to-run transition onset.

	Ace1[a]	Vnm1[a]	Voltron[b]	Ace2[c]	Vnm2[c]	Positron[b]	pAce[c]	pAceR[c]	Archon1[d]	QuasAr6a[d]	QuasAr6b[d]	ASAP2[e]	ASAP3[e]	ASAP4b[f]	ASAP4e[f]
Activation Kinetics															
Fast component amplitude (%)	60*	60*	61	67	68	85	82	54	93	96	100	77	81	19	14
Fast time constant (ms)	0.81	0.88	0.64	0.77	0.5	0.63	0.51	2.4	2.5	2.6	1.8	7	3.7	2.6	3.9
Slow time constant (ms)	4.6	5.2	4.1	3.1	1.9	19	1.5	5.4	13	21	0	79	48	21.2	20.6
Deactivation Kinetics															
Fast component amplitude (%)	60*	60*	55	65	72	90	78	58	94	98	96	65	81	8.8	20.6
Fast time constant (ms)	0.77	0.8	0.78	0.81	0.48	0.64	0.61	1.9	2	2.1	1.7	16.7	16	5.7	8.4
Slow time constant (ms)	5.2	4.7	3.9	2.8	3.1	37	3.2	7.2	17	31	22	116	102	24.5	17.5
Voltage Sensitivity															
ΔF/F per 100-mV step (%)	-11.6	-11.8	-20	-26.1	-19.1	20	30.5	27.8	70	73	24	-36	-51	180	210

Table S1 | Response kinetics and voltage sensitivities of GEVIs.
All kinetics parameters are from 1-photon measurements at 22°C in spiking HEK cells. Values have been extracted from the following publications: (a) Kannan *et al*, Nature Methods, 2018 (*18*); (b) Abdelfattah *et al*, Nature Communications, 2020 (*14*); (c) this study; (d) Tian *et al*, BioRxiv, 2021 (*87*); (e) Villette *et al*, Cell, 2019 (*20*); (f) Evans *et al*, BioRxiv 2021 (*88*). (*) amplitudes were not estimated in (a) and approximate values were taken from (e).
For indicators reported in this study, responses to depolarizing voltage steps obtained from transfected HEK cells were fitted using a biexponential step function to determine mean rise and decay kinetics. Imaging conditions: 505 nm LED for Ace-mNeon2 and pAce and 565 nm LED for VARNAM2 and pAceR, 25 mW mm^{-2} at sample plane; image acquisition: 5 kHz. n=6 cells for Ace-mNeon2, 7 cells for pAce, 4 cells each for VARNAM2 and pAceR.

References and Notes

1. K. A. Ferguson, J. A. Cardin, Mechanisms underlying gain modulation in the cortex. *Nat. Rev. Neurosci.* **21**, 80–92 (2020). doi:10.1038/s41583-019-0253-y Medline

2. Y. Fu, J. M. Tucciarone, J. S. Espinosa, N. Sheng, D. P. Darcy, R. A. Nicoll, Z. J. Huang, M. P. Stryker, A cortical circuit for gain control by behavioral state. *Cell* **156**, 1139–1152 (2014). doi:10.1016/j.cell.2014.01.050 Medline

3. C. C. Y. Lee, E. Kheradpezhouh, M. E. Diamond, E. Arabzadeh, State-dependent changes in perception and coding in the mouse somatosensory cortex. *Cell Rep.* **32**, 108197 (2020). doi:10.1016/j.celrep.2020.108197 Medline

4. P.-O. Polack, J. Friedman, P. Golshani, Cellular mechanisms of brain state-dependent gain modulation in visual cortex. *Nat. Neurosci.* **16**, 1331–1339 (2013). doi:10.1038/nn.3464 Medline

5. J. Schiemann, P. Puggioni, J. Dacre, M. Pelko, A. Domanski, M. C. W. van Rossum, I. Duguid, Cellular mechanisms underlying behavioral state-dependent bidirectional modulation of motor cortex output. *Cell Rep.* **11**, 1319–1330 (2015). doi:10.1016/j.celrep.2015.04.042 Medline

6. B. K. Hulse, E. V. Lubenov, A. G. Siapas, Brain state dependence of hippocampal subthreshold activity in awake mice. *Cell Rep.* **18**, 136–147 (2017). doi:10.1016/j.celrep.2016.11.084 Medline

7. P. Rajasethupathy, S. Sankaran, J. H. Marshel, C. K. Kim, E. Ferenczi, S. Y. Lee, A. Berndt, C. Ramakrishnan, A. Jaffe, M. Lo, C. Liston, K. Deisseroth, Projections from neocortex mediate top-down control of memory retrieval. *Nature* **526**, 653–659 (2015). doi:10.1038/nature15389 Medline

8. K. Q. Shan, E. V. Lubenov, M. Papadopoulou, A. G. Siapas, Spatial tuning and brain state account for dorsal hippocampal CA1 activity in a non-spatial learning task. *eLife* **5**, e14321 (2016). doi:10.7554/eLife.14321 Medline

9. C. Xu, S. Krabbe, J. Gründemann, P. Botta, J. P. Fadok, F. Osakada, D. Saur, B. F. Grewe, M. J. Schnitzer, E. M. Callaway, A. Lüthi, Distinct hippocampal pathways mediate dissociable roles of context in memory retrieval. *Cell* **167**, 961–972.e16 (2016). doi:10.1016/j.cell.2016.09.051 Medline

10. M. Kannan, G. Vasan, V. A. Pieribone, Optimizing strategies for developing genetically encoded voltage indicators. *Front. Cell. Neurosci.* **13**, 53 (2019). doi:10.3389/fncel.2019.00053 Medline

11. T. Knöpfel, C. Song, Optical voltage imaging in neurons: Moving from technology development to practical tool. *Nat. Rev. Neurosci.* **20**, 719–727 (2019). doi:10.1038/s41583-019-0231-4 Medline

12. H. H. Yang, F. St-Pierre, Genetically encoded voltage indicators: Opportunities and challenges. *J. Neurosci.* **36**, 9977–9989 (2016). doi:10.1523/JNEUROSCI.1095-16.2016 Medline

13. A. S. Abdelfattah, T. Kawashima, A. Singh, O. Novak, H. Liu, Y. Shuai, Y.-C. Huang, L. Campagnola, S. C. Seeman, J. Yu, J. Zheng, J. B. Grimm, R. Patel, J. Friedrich, B. D. Mensh, L. Paninski, J. J. Macklin, G. J. Murphy, K. Podgorski, B.-J. Lin, T.-W. Chen, G. C. Turner, Z. Liu, M. Koyama, K. Svoboda, M. B. Ahrens, L. D. Lavis, E. R. Schreiter, Bright and photostable chemigenetic indicators for extended in vivo voltage imaging. *Science* **365**, 699–704 (2019). doi:10.1126/science.aav6416 Medline

14. A. S. Abdelfattah, R. Valenti, J. Zheng, A. Wong, K. Podgorski, M. Koyama, D. S. Kim, E. R. Schreiter, GENIE Project Team, A general approach to engineer positive-going eFRET voltage indicators. *Nat. Commun.* **11**, 3444 (2020). doi:10.1038/s41467-020-17322-1 Medline

15. S. Chamberland, H. H. Yang, M. M. Pan, S. W. Evans, S. Guan, M. Chavarha, Y. Yang, C. Salesse, H. Wu, J. C. Wu, T. R. Clandinin, K. Toth, M. Z. Lin, F. St-Pierre, Fast two-photon imaging of subcellular voltage dynamics in neuronal tissue with genetically encoded indicators. *eLife* **6**, e25690 (2017). doi:10.7554/eLife.25690 Medline

16. L. Z. Fan, S. Kheifets, U. L. Böhm, H. Wu, K. D. Piatkevich, M. E. Xie, V. Parot, Y. Ha, K. E. Evans, E. S. Boyden, A. E. Takesian, A. E. Cohen, All-optical electrophysiology reveals the role of lateral inhibition in sensory processing in cortical layer 1. *Cell* **180**, 521–535.e18 (2020). doi:10.1016/j.cell.2020.01.001 Medline

17. Y. Gong, C. Huang, J. Z. Li, B. F. Grewe, Y. Zhang, S. Eismann, M. J. Schnitzer, High-speed recording of neural spikes in awake mice and flies with a fluorescent voltage sensor. *Science* **350**, 1361–1366 (2015). doi:10.1126/science.aab0810 Medline

18. M. Kannan, G. Vasan, C. Huang, S. Haziza, J. Z. Li, H. Inan, M. J. Schnitzer, V. A. Pieribone, Fast, in vivo voltage imaging using a red fluorescent indicator. *Nat. Methods* **15**, 1108–1116 (2018). doi:10.1038/s41592-018-0188-7 Medline

19. K. D. Piatkevich, E. E. Jung, C. Straub, C. Linghu, D. Park, H.-J. Suk, D. R. Hochbaum, D. Goodwin, E. Pnevmatikakis, N. Pak, T. Kawashima, C.-T. Yang, J. L. Rhoades, O. Shemesh, S. Asano, Y.-G. Yoon, L. Freifeld, J. L. Saulnier, C. Riegler, F. Engert, T. Hughes, M. Drobizhev, B. Szabo, M. B. Ahrens, S. W. Flavell, B. L. Sabatini, E. S. Boyden, A robotic multidimensional directed evolution approach applied to fluorescent voltage reporters. *Nat. Chem. Biol.* **14**, 352–360 (2018). doi:10.1038/s41589-018-0004-9 Medline

20. V. Villette, M. Chavarha, I. K. Dimov, J. Bradley, L. Pradhan, B. Mathieu, S. W. Evans, S. Chamberland, D. Shi, R. Yang, B. B. Kim, A. Ayon, A. Jalil, F. St-Pierre, M. J. Schnitzer, G. Bi, K. Toth, J. Ding, S. Dieudonné, M. Z. Lin, Ultrafast two-photon imaging of a high-gain voltage indicator in awake behaving mice. *Cell* **179**, 1590–1608.e23 (2019). doi:10.1016/j.cell.2019.11.004 Medline

21. H. H. Yang, F. St-Pierre, X. Sun, X. Ding, M. Z. Lin, T. R. Clandinin, Subcellular imaging of voltage and calcium signals reveals neural processing in vivo. *Cell* **166**, 245–257 (2016). doi:10.1016/j.cell.2016.05.031 Medline

22. Y. Adam, J. J. Kim, S. Lou, Y. Zhao, M. E. Xie, D. Brinks, H. Wu, M. A. Mostajo-Radji, S. Kheifets, V. Parot, S. Chettih, K. J. Williams, B. Gmeiner, S. L. Farhi, L. Madisen, E. K. Buchanan, I. Kinsella, D. Zhou, L. Paninski, C. D. Harvey, H. Zeng, P. Arlotta, R. E.

Campbell, A. E. Cohen, Voltage imaging and optogenetics reveal behaviour-dependent changes in hippocampal dynamics. *Nature* **569**, 413–417 (2019). doi:10.1038/s41586-019-1166-7 Medline

23. K. D. Piatkevich, S. Bensussen, H. A. Tseng, S. N. Shroff, V. G. Lopez-Huerta, D. Park, E. E. Jung, O. A. Shemesh, C. Straub, H. J. Gritton, M. F. Romano, E. Costa, B. L. Sabatini, Z. Fu, E. S. Boyden, X. Han, Population imaging of neural activity in awake behaving mice. *Nature* **574**, 413–417 (2019). doi:10.1038/s41586-019-1641-1 Medline

24. S. Xiao, E. Lowet, H. J. Gritton, P. Fabris, Y. Wang, J. Sherman, R. A. Mount, H. A. Tseng, H.-Y. Man, C. Straub, K. D. Piatkevich, E. S. Boyden, J. Mertz, X. Han, Large-scale voltage imaging in behaving mice using targeted illumination. *iScience* **24**, 103263 (2021). doi:10.1016/j.isci.2021.103263 Medline

25. Y. Gong, M. J. Wagner, J. Zhong Li, M. J. Schnitzer, Imaging neural spiking in brain tissue using FRET-opsin protein voltage sensors. *Nat. Commun.* **5**, 3674 (2014). doi:10.1038/ncomms4674 Medline

26. P. Zou, Y. Zhao, A. D. Douglass, D. R. Hochbaum, D. Brinks, C. A. Werley, D. J. Harrison, R. E. Campbell, A. E. Cohen, Bright and fast multicoloured voltage reporters via electrochromic FRET. *Nat. Commun.* **5**, 4625 (2014). doi:10.1038/ncomms5625 Medline

27. D. R. Hochbaum, Y. Zhao, S. L. Farhi, N. Klapoetke, C. A. Werley, V. Kapoor, P. Zou, J. M. Kralj, D. Maclaurin, N. Smedemark-Margulies, J. L. Saulnier, G. L. Boulting, C. Straub, Y. K. Cho, M. Melkonian, G. K.-S. Wong, D. J. Harrison, V. N. Murthy, B. L. Sabatini, E. S. Boyden, R. E. Campbell, A. E. Cohen, All-optical electrophysiology in mammalian neurons using engineered microbial rhodopsins. *Nat. Methods* **11**, 825–833 (2014). doi:10.1038/nmeth.3000 Medline

28. N. C. Shaner, G. G. Lambert, A. Chammas, Y. Ni, P. J. Cranfill, M. A. Baird, B. R. Sell, J. R. Allen, R. N. Day, M. Israelsson, M. W. Davidson, J. Wang, A bright monomeric green fluorescent protein derived from *Branchiostoma lanceolatum*. *Nat. Methods* **10**, 407–409 (2013). doi:10.1038/nmeth.2413 Medline

29. B. T. Bajar, E. S. Wang, A. J. Lam, B. B. Kim, C. L. Jacobs, E. S. Howe, M. W. Davidson, M. Z. Lin, J. Chu, Improving brightness and photostability of green and red fluorescent proteins for live cell imaging and FRET reporting. *Sci. Rep.* **6**, 20889 (2016). doi:10.1038/srep20889 Medline

30. J. Park, C. A. Werley, V. Venkatachalam, J. M. Kralj, S. D. Dib-Hajj, S. G. Waxman, A. E. Cohen, Screening fluorescent voltage indicators with spontaneously spiking HEK cells. *PLOS ONE* **8**, e85221 (2013). doi:10.1371/journal.pone.0085221 Medline

31. H. Zhang, E. Reichert, A. E. Cohen, Optical electrophysiology for probing function and pharmacology of voltage-gated ion channels. *eLife* **5**, e15202 (2016). doi:10.7554/eLife.15202 Medline

32. L. Stryer, Fluorescence energy transfer as a spectroscopic ruler. *Annu. Rev. Biochem.* **47**, 819–846 (1978). doi:10.1146/annurev.bi.47.070178.004131 Medline

33. T. Kikukawa, K. Shimono, J. Tamogami, S. Miyauchi, S. Y. Kim, T. Kimura-Someya, M. Shirouzu, K.-H. Jung, S. Yokoyama, N. Kamo, Photochemistry of *Acetabularia*

rhodopsin II from a marine plant, *Acetabularia acetabulum*. *Biochemistry* **50**, 8888–8898 (2011). doi:10.1021/bi2009932 Medline

34. T. Wada, K. Shimono, T. Kikukawa, M. Hato, N. Shinya, S. Y. Kim, T. Kimura-Someya, M. Shirouzu, J. Tamogami, S. Miyauchi, K.-H. Jung, N. Kamo, S. Yokoyama, Crystal structure of the eukaryotic light-driven proton-pumping rhodopsin, *Acetabularia* rhodopsin II, from marine alga. *J. Mol. Biol.* **411**, 986–998 (2011). doi:10.1016/j.jmb.2011.06.028 Medline

35. D. Maclaurin, V. Venkatachalam, H. Lee, A. E. Cohen, Mechanism of voltage-sensitive fluorescence in a microbial rhodopsin. *Proc. Natl. Acad. Sci. U.S.A.* **110**, 5939–5944 (2013). doi:10.1073/pnas.1215595110 Medline

36. L. Zimányi, G. Váró, M. Chang, B. Ni, R. Needleman, J. K. Lanyi, Pathways of proton release in the bacteriorhodopsin photocycle. *Biochemistry* **31**, 8535–8543 (1992). doi:10.1021/bi00151a022 Medline

37. J. Platisa, G. Vasan, A. Yang, V. A. Pieribone, Directed evolution of key residues in fluorescent protein inverses the polarity of voltage sensitivity in the genetically encoded indicator ArcLight. *ACS Chem. Neurosci.* **8**, 513–523 (2017). doi:10.1021/acschemneuro.6b00234 Medline

38. B. A. Wilt, J. E. Fitzgerald, M. J. Schnitzer, Photon shot noise limits on optical detection of neuronal spikes and estimation of spike timing. *Biophys. J.* **104**, 51–62 (2013). doi:10.1016/j.bpj.2012.07.058 Medline

39. M. E. Garrett, I. Nauhaus, J. H. Marshel, E. M. Callaway, Topography and areal organization of mouse visual cortex. *J. Neurosci.* **34**, 12587–12600 (2014). doi:10.1523/JNEUROSCI.1124-14.2014 Medline

40. H. Taniguchi, M. He, P. Wu, S. Kim, R. Paik, K. Sugino, D. Kvitsiani, Y. Fu, J. Lu, Y. Lin, G. Miyoshi, Y. Shima, G. Fishell, S. B. Nelson, Z. J. Huang, A resource of Cre driver lines for genetic targeting of GABAergic neurons in cerebral cortex. *Neuron* **71**, 995–1013 (2011). doi:10.1016/j.neuron.2011.07.026 Medline

41. B. Tasic, V. Menon, T. N. Nguyen, T. K. Kim, T. Jarsky, Z. Yao, B. Levi, L. T. Gray, S. A. Sorensen, T. Dolbeare, D. Bertagnolli, J. Goldy, N. Shapovalova, S. Parry, C. Lee, K. Smith, A. Bernard, L. Madisen, S. M. Sunkin, M. Hawrylycz, C. Koch, H. Zeng, Adult mouse cortical cell taxonomy revealed by single cell transcriptomics. *Nat. Neurosci.* **19**, 335–346 (2016). doi:10.1038/nn.4216 Medline

42. J. Zhuang, L. Ng, D. Williams, M. Valley, Y. Li, M. Garrett, J. Waters, An extended retinotopic map of mouse cortex. *eLife* **6**, e18372 (2017). doi:10.7554/eLife.18372 Medline

43. S. T. Lim, D. E. Antonucci, R. H. Scannevin, J. S. Trimmer, A novel targeting signal for proximal clustering of the Kv2.1 K^+ channel in hippocampal neurons. *Neuron* **25**, 385–397 (2000). doi:10.1016/S0896-6273(00)80902-2 Medline

44. C. Cai, J. Friedrich, A. Singh, M. H. Eybposh, E. A. Pnevmatikakis, K. Podgorski, A. Giovannucci, VolPy: Automated and scalable analysis pipelines for voltage imaging

datasets. *PLOS Comput. Biol.* **17**, e1008806 (2021). doi:10.1371/journal.pcbi.1008806 Medline

45. H. Inan, M. A. Erdogdu, M. J. Schnitzer, "Robust estimation of neural signals in calcium imaging" in *NIPS'17: Proceedings of the 31st International Conference on Neural Information Processing Systems*, U. von Luxburg, I. Guyon, S. Bengio, H. Wallach, R. Fergus, S. V. N. Vishwanathan, R. Garnett, Eds. (Curran Associates Inc., 2017).

46. H. Inan, C. Schmuckermair, T. Tasci, B. O. Ahanonu, O. Hernandez, J. Lecoq, F. Dinç, M. J. Wagner, M. A. Erdogdu, M. J. Schnitzer, Fast and statistically robust cell extraction from large-scale neural calcium imaging datasets. bioRxiv 2021.2003.2024.436279 [Preprint] (2021); https://doi.org/10.1101/2021.03.24.436279.

47. E. Abs, R. B. Poorthuis, D. Apelblat, K. Muhammad, M. B. Pardi, L. Enke, D. Kushinsky, D.-L. Pu, M. F. Eizinger, K.-K. Conzelmann, I. Spiegel, J. J. Letzkus, Learning-related plasticity in dendrite-targeting layer 1 interneurons. *Neuron* **100**, 684–699.e6 (2018). doi:10.1016/j.neuron.2018.09.001 Medline

48. K. Cohen-Kashi Malina, E. Tsivourakis, D. Kushinsky, D. Apelblat, S. Shtiglitz, E. Zohar, M. Sokoletsky, G. Tasaka, A. Mizrahi, I. Lampl, I. Spiegel, NDNF interneurons in layer 1 gain-modulate whole cortical columns according to an animal's behavioral state. *Neuron* **109**, 2150–2164.e5 (2021). doi:10.1016/j.neuron.2021.05.001 Medline

49. M. He, J. Tucciarone, S. Lee, M. J. Nigro, Y. Kim, J. M. Levine, S. M. Kelly, I. Krugikov, P. Wu, Y. Chen, L. Gong, Y. Hou, P. Osten, B. Rudy, Z. J. Huang, Strategies and tools for combinatorial targeting of GABAergic neurons in mouse cerebral cortex. *Neuron* **92**, 555 (2016). doi:10.1016/j.neuron.2016.10.009 Medline

50. H. Adesnik, W. Bruns, H. Taniguchi, Z. J. Huang, M. Scanziani, A neural circuit for spatial summation in visual cortex. *Nature* **490**, 226–231 (2012). doi:10.1038/nature11526 Medline

51. L. Mesik, W. P. Ma, L. Y. Li, L. A. Ibrahim, Z. J. Huang, L. I. Zhang, H. W. Tao, Functional response properties of VIP-expressing inhibitory neurons in mouse visual and auditory cortex. *Front. Neural Circuits* **9**, 22 (2015). doi:10.3389/fncir.2015.00022 Medline

52. J. Yu, H. Hu, A. Agmon, K. Svoboda, Recruitment of GABAergic interneurons in the barrel cortex during active tactile behavior. *Neuron* **104**, 412–427.e4 (2019). doi:10.1016/j.neuron.2019.07.027 Medline

53. M. Vinck, R. Batista-Brito, U. Knoblich, J. A. Cardin, Arousal and locomotion make distinct contributions to cortical activity patterns and visual encoding. *Neuron* **86**, 740–754 (2015). doi:10.1016/j.neuron.2015.03.028 Medline

54. J. Reimer, E. Froudarakis, C. R. Cadwell, D. Yatsenko, G. H. Denfield, A. S. Tolias, Pupil fluctuations track fast switching of cortical states during quiet wakefulness. *Neuron* **84**, 355–362 (2014). doi:10.1016/j.neuron.2014.09.033 Medline

55. C. K. Pfeffer, M. Xue, M. He, Z. J. Huang, M. Scanziani, Inhibition of inhibition in visual cortex: The logic of connections between molecularly distinct interneurons. *Nat. Neurosci.* **16**, 1068–1076 (2013). doi:10.1038/nn.3446 Medline

56. U. Knoblich, L. Huang, H. Zeng, L. Li, Neuronal cell-subtype specificity of neural synchronization in mouse primary visual cortex. *Nat. Commun.* **10**, 2533 (2019). doi:10.1038/s41467-019-10498-1 Medline

57. L. Cossell, M. F. Iacaruso, D. R. Muir, R. Houlton, E. N. Sader, H. Ko, S. B. Hofer, T. D. Mrsic-Flogel, Functional organization of excitatory synaptic strength in primary visual cortex. *Nature* **518**, 399–403 (2015). doi:10.1038/nature14182 Medline

58. J. Akerboom, N. Carreras Calderón, L. Tian, S. Wabnig, M. Prigge, J. Tolö, A. Gordus, M. B. Orger, K. E. Severi, J. J. Macklin, R. Patel, S. R. Pulver, T. J. Wardill, E. Fischer, C. Schüler, T.-W. Chen, K. S. Sarkisyan, J. S. Marvin, C. I. Bargmann, D. S. Kim, S. Kügler, L. Lagnado, P. Hegemann, A. Gottschalk, E. R. Schreiter, L. L. Looger, Genetically encoded calcium indicators for multi-color neural activity imaging and combination with optogenetics. *Front. Mol. Neurosci.* **6**, 2 (2013). doi:10.3389/fnmol.2013.00002 Medline

59. H. Dana, B. Mohar, Y. Sun, S. Narayan, A. Gordus, J. P. Hasseman, G. Tsegaye, G. T. Holt, A. Hu, D. Walpita, R. Patel, J. J. Macklin, C. I. Bargmann, M. B. Ahrens, E. R. Schreiter, V. Jayaraman, L. L. Looger, K. Svoboda, D. S. Kim, Sensitive red protein calcium indicators for imaging neural activity. *eLife* **5**, e12727 (2016). doi:10.7554/eLife.12727 Medline

60. M. Inoue, A. Takeuchi, S. Horigane, M. Ohkura, K. Gengyo-Ando, H. Fujii, S. Kamijo, S. Takemoto-Kimura, M. Kano, J. Nakai, K. Kitamura, H. Bito, Rational design of a high-affinity, fast, red calcium indicator R-CaMP2. *Nat. Methods* **12**, 64–70 (2015). doi:10.1038/nmeth.3185 Medline

61. M. Inoue, A. Takeuchi, S. Manita, S. I. Horigane, M. Sakamoto, R. Kawakami, K. Yamaguchi, K. Otomo, H. Yokoyama, R. Kim, T. Yokoyama, S. Takemoto-Kimura, M. Abe, M. Okamura, Y. Kondo, S. Quirin, C. Ramakrishnan, T. Imamura, K. Sakimura, T. Nemoto, M. Kano, H. Fujii, K. Deisseroth, K. Kitamura, H. Bito, Rational engineering of XCaMPs, a multicolor GECI suite for in vivo imaging of complex brain circuit dynamics. *Cell* **177**, 1346–1360.e24 (2019). doi:10.1016/j.cell.2019.04.007 Medline

62. M. M. Karnani, J. Jackson, I. Ayzenshtat, A. Hamzehei Sichani, K. Manoocheri, S. Kim, R. Yuste, Opening holes in the blanket of inhibition: Localized lateral disinhibition by VIP interneurons. *J. Neurosci.* **36**, 3471–3480 (2016). doi:10.1523/JNEUROSCI.3646-15.2016 Medline

63. W. Akemann, H. Mutoh, A. Perron, Y. K. Park, Y. Iwamoto, T. Knöpfel, Imaging neural circuit dynamics with a voltage-sensitive fluorescent protein. *J. Neurophysiol.* **108**, 2323–2337 (2012). doi:10.1152/jn.00452.2012 Medline

64. F. Li, J. W. Lindsey, E. C. Marin, N. Otto, M. Dreher, G. Dempsey, I. Stark, A. S. Bates, M. W. Pleijzier, P. Schlegel, A. Nern, S. Y. Takemura, N. Eckstein, T. Yang, A. Francis, A. Braun, R. Parekh, M. Costa, L. K. Scheffer, Y. Aso, G. S. X. E. Jefferis, L. F. Abbott, A. Litwin-Kumar, S. Waddell, G. M. Rubin, The connectome of the adult Drosophila mushroom body provides insights into function. *eLife* **9**, e62576 (2020). doi:10.7554/eLife.62576 Medline

65. J. Jackson, I. Ayzenshtat, M. M. Karnani, R. Yuste, VIP+ interneurons control neocortical activity across brain states. *J. Neurophysiol.* **115**, 3008–3017 (2016). doi:10.1152/jn.01124.2015 Medline

66. J. Reimer, M. J. McGinley, Y. Liu, C. Rodenkirch, Q. Wang, D. A. McCormick, A. S. Tolias, Pupil fluctuations track rapid changes in adrenergic and cholinergic activity in cortex. *Nat. Commun.* **7**, 13289 (2016). doi:10.1038/ncomms13289 Medline

67. J. M. P. Pakan, S. C. Lowe, E. Dylda, S. W. Keemink, S. P. Currie, C. A. Coutts, N. L. Rochefort, Behavioral-state modulation of inhibition is context-dependent and cell type specific in mouse visual cortex. *eLife* **5**, e14985 (2016). doi:10.7554/eLife.14985 Medline

68. S. Xiao, H. A. Tseng, H. Gritton, X. Han, J. Mertz, Video-rate volumetric neuronal imaging using 3D targeted illumination. *Sci. Rep.* **8**, 7921 (2018). doi:10.1038/s41598-018-26240-8 Medline

69. M. L. Andermann, N. B. Gilfoy, G. J. Goldey, R. N. S. Sachdev, M. Wölfel, D. A. McCormick, R. C. Reid, M. J. Levene, Chronic cellular imaging of entire cortical columns in awake mice using microprisms. *Neuron* **80**, 900–913 (2013). doi:10.1016/j.neuron.2013.07.052 Medline

70. J. C. Jung, A. D. Mehta, E. Aksay, R. Stepnoski, M. J. Schnitzer, In vivo mammalian brain imaging using one- and two-photon fluorescence microendoscopy. *J. Neurophysiol.* **92**, 3121–3133 (2004). doi:10.1152/jn.00234.2004 Medline

71. R. P. Barretto, B. Messerschmidt, M. J. Schnitzer, In vivo fluorescence imaging with high-resolution microlenses. *Nat. Methods* **6**, 511–512 (2009). doi:10.1038/nmeth.1339 Medline

72. R. P. Barretto, M. J. Schnitzer, In vivo optical microendoscopy for imaging cells lying deep within live tissue. *Cold Spring Harb. Protoc.* **2012**, 1029–1034 (2012). doi:10.1101/pdb.top071464 Medline

73. Allen Institute for Brain Science, Cell types: Overview of the data, Allen cell types database; https://celltypes.brain-map.org/.

74. G. Buzsáki, C. A. Anastassiou, C. Koch, The origin of extracellular fields and currents—EEG, ECoG, LFP and spikes. *Nat. Rev. Neurosci.* **13**, 407–420 (2012). doi:10.1038/nrn3241 Medline

75. I. Soltesz, A. Losonczy, CA1 pyramidal cell diversity enabling parallel information processing in the hippocampus. *Nat. Neurosci.* **21**, 484–493 (2018). doi:10.1038/s41593-018-0118-0 Medline

76. L. Jin, Z. Han, J. Platisa, J. R. A. Wooltorton, L. B. Cohen, V. A. Pieribone, Single action potentials and subthreshold electrical events imaged in neurons with a fluorescent protein voltage probe. *Neuron* **75**, 779–785 (2012). doi:10.1016/j.neuron.2012.06.040 Medline

77. C. Huang, J. R. Maxey, S. Sinha, J. Savall, Y. Gong, M. J. Schnitzer, Long-term optical brain imaging in live adult fruit flies. *Nat. Commun.* **9**, 872 (2018). doi:10.1038/s41467-018-02873-1 Medline

78. G. J. Goldey, D. K. Roumis, L. L. Glickfeld, A. M. Kerlin, R. C. Reid, V. Bonin, D. P. Schafer, M. L. Andermann, Removable cranial windows for long-term imaging in awake mice. *Nat. Protoc.* **9**, 2515–2538 (2014). doi:10.1038/nprot.2014.165 Medline

79. P. Thévenaz, U. E. Ruttimann, M. Unser, A pyramid approach to subpixel registration based on intensity. *IEEE Trans. Image Process.* **7**, 27–41 (1998). doi:10.1109/83.650848 Medline

80. E. A. Pnevmatikakis, A. Giovannucci, NoRMCorre: An online algorithm for piecewise rigid motion correction of calcium imaging data. *J. Neurosci. Methods* **291**, 83–94 (2017). doi:10.1016/j.jneumeth.2017.07.031 Medline

81. K. He, G. Gkioxari, P. Dollar, R. Girshick, Mask R-CNN. *IEEE Trans. Pattern Anal. Mach. Intell.* **42**, 386–397 (2020). doi:10.1109/TPAMI.2018.2844175 Medline

82. F. Franke, R. Quian Quiroga, A. Hierlemann, K. Obermayer, Bayes optimal template matching for spike sorting - combining fisher discriminant analysis with optimal filtering. *J. Comput. Neurosci.* **38**, 439–459 (2015). doi:10.1007/s10827-015-0547-7 Medline

83. E. A. Pnevmatikakis, D. Soudry, Y. Gao, T. A. Machado, J. Merel, D. Pfau, T. Reardon, Y. Mu, C. Lacefield, W. Yang, M. Ahrens, R. Bruno, T. M. Jessell, D. S. Peterka, R. Yuste, L. Paninski, Simultaneous denoising, deconvolution, and demixing of calcium imaging data. *Neuron* **89**, 285–299 (2016). doi:10.1016/j.neuron.2015.11.037 Medline

84. E. A. Mukamel, A. Nimmerjahn, M. J. Schnitzer, Automated analysis of cellular signals from large-scale calcium imaging data. *Neuron* **63**, 747–760 (2009). doi:10.1016/j.neuron.2009.08.009 Medline

85. T. Deneux, A. Kaszas, G. Szalay, G. Katona, T. Lakner, A. Grinvald, B. Rózsa, I. Vanzetta, Accurate spike estimation from noisy calcium signals for ultrafast three-dimensional imaging of large neuronal populations in vivo. *Nat. Commun.* **7**, 12190 (2016). doi:10.1038/ncomms12190 Medline

86. M. Kannan, G. Vasan, S. Haziza, C. Huang, R. Chrapkiewicz, J. Luo, J. A. Cardin, M. J. Schnitzer, V. A. Pieribone, Dual-polarity voltage imaging of the concurrent activation dynamics of multiple neuron types. Zenodo (2022); https://doi.org/10.5281/zenodo.6361012.

87. H. Tian, H. C. Davis, J. D. Wong-Campos, L. Z. Fan, B. Gmeiner, S. Begum, C. A. Werley, G. B. Borja, H. Upadhyay, H. Shah, J. Jacques, P. Park, Y. Qi, V. Parot, K. Deisseroth, A. E. Cohen, All-optical electrophysiology with improved genetically encoded voltage indicators reveals interneuron network dynamics in vivo. bioRxiv 2021.11.22.469481 [Preprint] 2021; https://doi.org/10.1101/2021.11.22.469481.

88. S. W. Evans, D. Shi, M. Chavarha, M. H. Plitt, J. Taxidis, B. Madruga, S. C. van Keulen, M. M. Pang, S. Su, F.-J. Hwang, G. Zhang, A. Reese, L. Pradhan, J. L. Fan, S. Lee, Y. Liu, C.-M. Suomivuori, D. Jiang, A. Negrean, S. Wang, N. Ji, T. R. Clandinin, R. O. Dror, G. Bi, C. D. Makinson, P. Golshani, L. M. Giocomo, A. Losonczy, J. B. Ding, M. Z. Lin, A positively tuned voltage indicator reveals electrical correlates of calcium activity in the brain. bioRxiv 2021.10.21.465345 [Preprint] 2021; https://doi.org/10.1101/2021.10.21.465345.